Investigating flood processes in karst catchments by combining concentration-discharge relationship analysis and lateral flow simulation

Martin Le Mesnil, Jean-Baptiste Charlier, Roger Moussa, Yvan Caballero

Investigating flood processes in karst catchments by combining Concentration-Discharge relationship analysis and lateral flow simulation

Martin Le Mesnil[1,2,3], Jean-Baptiste Charlier[1,2], Roger Moussa[3] and Yvan Caballero[1,2]

[1] BRGM, Univ. Montpellier, Montpellier, France.

[2] G-eau, INRAE, CIRAD, IRD, AgroParisTech, Supagro, BRGM, Montpellier, France.

[3] LISAH, Univ. Montpellier, INRAE, IRD, Montpellier SupAgro, Montpellier, France.

Corresponding author: Martin Le Mesnil (martin.lemesnil@gmail.com)

Keywords: Concentration-discharge, karst, storm, hysteresis, lateral flow

1 Introduction

Runoff at the catchment outlet has different origins depending on the water flow paths in the surface, subsurface, and underground compartments. The joint study of hydrological and hydrochemical signals through concentration-discharge (C-Q) relationships can help improving our understanding of these origins and associated hydrological processes. Depending on the context and nature of investigations, C-Q relationship analysis can be applied to different variables, the most frequently monitored parameters being major ions or continuous physico-chemical variables such as electrical conductivity, turbidity, alkalinity, or pH (e.g. Rose, 2003). A synthesis by Knapp et al. (2020), based on results obtained in a Swiss mountainous catchment,

15 summarizes the main environmental drivers of C-Q relationships at the storm-event and longer
16 time scales. The main approaches encountered in the literature for the study of these
17 relationships are end-member mixing analysis (Burns et al., 2001; Doctor et al., 2006), statistical
18 approaches (Anderson et al., 1997) and hysteresis studies (Evans and Davies, 1998; Evans et al.,
19 1999; Rose, 2003; Rose et al., 2018). They led to advances in the understanding of aquifer
20 recharge and vulnerability (House and Warwick, 1998; Huebsch et al., 2014), streamflow
21 contributions (Ribolzi et al., 2000), and storm-event spring discharge (Toran and Reisch, 2012).
22 Most C-Q analyses are interpreted in terms of a two-component system involving pre-event
23 water (PEW) and event water (EW) (Evans et al., 1999; Rose, 2003), or include a third
24 component defined as soil or rapid infiltration water (Evans and Davies, 1998; Ribolzi et al.,
25 2000, Burns et al., 2001; Toran and Reisch, 2012). While most C-Q studies use the concentration
26 values of different streamflow source to perform the hydrograph separation, some use an *a priori*
27 separation to infer source concentration values (Neira et al., 2020).

28 At the catchment scale, hysteresis analyses allow studying C-Q relationships, using C and
29 Q data at a given monitoring station. Hysteresis loops are mainly characterized using
30 classifications of loop shapes, such as the widely used 6-type proposed by Evans and Davies
31 (1998), or more recent 9-type ones (Butturini et al., 2008; Heathwaite and Bieroza, 2020) using
32 hysteresis indices (see a synthesis by Lloyd et al., 2016). These approaches make it possible to
33 investigate streamflow contributions during storm events, knowing concentration ranking of
34 supposed end-members (Rose, 2003; Vaughan et al., 2017). When monitoring several gauging
35 stations for Q and C along the stream, it is possible to assess C-Q relationship spatial variability
36 at nested catchment scale. It is also possible to characterize it based on a reach scale approach

(between two gauging stations). In that case, water origin and flood hydrological processes can be investigated by analyzing lateral exchanges, i.e. stream water gains or losses from or to groundwater. Such analyses were performed by Covino et al. (2011) and Mallard et al. (2014), using artificial tracing experiments to investigate stream composition changes. Analytical approaches also exist, such as the advection-diffusion equation (ADE), widely used to model conservative solute transport (Runkel, 1996; Baeumer et al., 2001; Hauns et al., 2001; Luhmann et al., 2012). This equation is mathematically similar to the diffusive wave equation (DWE) and both can be resolved using the Hayami analytical solution (1951), making it possible to simulate lateral flows Q and C (Cholet et al., 2017).

Karst catchments are located in carbonate areas (including limestone and dolomite) and cover 20% of Europe land surface and 35 % in France (Goldscheider et al., 2020). They are known to be complex permeable hydrosystems, involving high rainfall infiltration rates through open conduits and promoting fast groundwater flow and significant surface water-groundwater interaction (Bakalowicz, 2005). In such areas, electrical conductivity (EC) provides information on groundwater residence time and water origin, as it is controlled by bicarbonate, calcium, and magnesium concentrations resulting from carbonate rock dissolution (Hess and White, 1988; Lambán et al., 2015; Liu et al., 2007). Because EC can be easily monitored at high-frequency time steps, it is a useful variable for the characterization of C-Q relationships, particularly in karst catchments. Indeed, the contrast between water end-members is notable: low-mineralization EW from surface runoff or fast groundwater flow, and high-mineralization PEW from groundwater present in the aquifer prior to the storm event. The range of EC values is variable, depending on groundwater residence time or mixing with fast rainwater infiltration, and

allow identifying PEW and EW occurrence. In the particular case of karst catchments, an additional challenge is to distinguish EW from direct surface runoff on low permeability areas and EW from fast infiltration in open conduits feeding rivers through springs (Hartmann et al., 2021). Moreover, unexpected EC variations can occur during high-flow periods, as groundwater boundaries extend and incorporate areas with different EC values (Ravbar et al., 2011).

Various methodologies have been used to explore EC-Q relationships during storm events in karst catchments. Early studies mainly describe EC variations during storm events, an EC drop being interpreted as an increasing EW contribution in streamflow, and complex fluctuations corresponding to several simultaneous karst conduit contributions (Hess and White, 1988). Statistically-based methods exist, such as EC frequency distribution analysis (Massei et al., 2007) which makes it possible to investigate the relative contributions of surface water and groundwater to streamflow and how they are influenced by hydrological conditions. Characterization of EC-Q hysteresis loops is also used, which makes it possible to study delays between discharge and solute concentration variations, bringing to light the changing hydrological processes at the scale of a storm event, or between different events (Fournier et al., 2007; Toran and Reisch, 2012). Hysteresis loops of hydrographs at different locations within a karst catchment were also studied to identify hydrological flows at nested catchment scale (Zhang et al., 2020). Analysis of EC and Q patterns at the storm-event time scale have also highlighted the importance of seasonal variability in the physico-chemical response of a karstic spring (Fournier et al., 2007). Recently, EC-Q relationships at the reach scale were studied by Cholet et al. (2017) using lateral exchange modeling to investigate conduit-matrix relationship variability during storm events according to seasons. Each methodology helps better

81 understanding hydrological processes, and we identify a strong interest in combining different
82 approaches and to investigate both nested and reach scales to improve the conceptual model of
83 karst catchments.

84 The aim of this article is to assess the potential of a combined approach to investigate the
85 spatio-temporal variability of flood processes within karst catchments. To do that, we combine
86 two spatial scales of investigation: at the nested catchment scale, a classification of C-Q
87 hysteresis loops adapted to EC measurement in karst context; at the reach scale, an inverse
88 modeling of lateral flow Q and C. Using this combined approach, we will define what can be
89 learned from C-Q hysteresis loop analysis in karst catchment storm events, and what additional
90 information can bring the modeling of lateral flow Q and C. To answer these questions, we apply
91 the two-step approach on hourly records of Q and EC during storm events at 4 gauging stations
92 in two karst catchments in France, characterized by contrasting climate and karst area extension.
93 Results are interpreted in terms of water origin using PEW and EW contributions during storm
94 events. Finally, conceptual models are proposed, that summarize the main information obtained
95 with the combined approach, regarding spatio-temporal variability of flood processes.

96 # 2 Methodology

97 ## *2.1 General methodology*

98 To propose a conceptual model of flood water origin spatio-temporal variability, a two-
99 part methodology was applied. The parts correspond to two spatial scales: i) the nested
100 catchment scale considering the topographic catchment upstream a gauging station, and ii) the
101 reach scale considering the catchment delimited by two gauging stations. Both parts rely on

hourly Q and C data collection during storm events, the difference being that reach scale analysis requires data from both inlet and outlet stations. To analyze temporal variability, the methodology was applied on storm-events grouped by seasons. Figure 1 presents this general methodology, from field measurement network and monitored variables to data processing.

At the nested catchment scale, C-Q loops are analyzed for each storm event according to the methodology described in section 2.2. This analysis is performed at each monitoring station of the hydrograph network and characterizes flood processes occurring in the whole upstream topographic catchment. It is thus a lumped approach at the catchment scale, and successive analyses towards the final outlet are interpreted in terms of flood process variability of nested catchments. Even so, a more spatially discrete approach at the reach scale is necessary to refine and spatialize this variability description.

At the reach scale, the hourly lateral flow discharge (Q_L) and concentration (C_L) variations are simulated using the DWE inverse model, detailed in section 2.3, assuming that exchanges are uniformly distributed along river reaches. Although this may not be the case in karst systems, this approach allows a more spatialized investigation of the location of lateral flows, which commonly lacks in C-Q studies. This reach-scale approach, consists in comparing obtained mean C_L values to PEW and EW end-member C values. More details regarding definitions of these end-members are given in section 3.3.

[Figure 1]

A season-based storm-event typology is proposed, which allows interpreting hydrological response variability. Four seasons are defined, based on typical hydrological dynamics of the

study sites: low water table and first storm events in September and October, high precipitation volume winter events from November to March, lower intensity events from April to May, and occasional summer storm events from June to August. Finally, a conceptual model that associates flood processes to different seasons and karst configurations is proposed, in addition to a schematic representation of the spatial variability of water origin along river reaches.

2.2 Nested catchment scale approach: C-Q loop analysis

This section presents a C-Q loop classification that allows characterizing hysteresis loops obtained from the monitoring of various physico-chemical parameters (concentration, turbidity, EC, …). Evans and Davies (1998) proposed a 6-type classification of C-Q loops based on the loop's general trend and its rotational direction. This classification was used in later C-Q studies (Rose, 2003; Vaughan et al., 2017; Zhang et al., 2020). Building on Evans and Davies (1998), we use a modified loop typology, enriched by the integration of a hysteresis index quantification and the inclusion of non-hysteresis pathways. Similar 9-type classifications have been proposed and shown to be relevant for C-Q relationship studies (Butturini et al., 2008; Heathwaite and Bieroza, 2020). We calculated two indicators for loop classification: slope (s), obtained by applying a linear regression to the C-Q values, and hysteresis index (HI).

The hysteresis index proposed by Lloyd et al. (2016) is used in this work. It provides information on both the loop direction and its amplitude. Moreover, it considers the whole range of discharge values and is calculated based on normalized Q and EC values, which facilitates consistent inter-event and inter-site comparison. For a given storm event, Q and EC values are

145 normalized between 0 and 1, and at each 5% interval (i) of normalized Q, a local HI_i is
146 calculated following eq. 1:

147 $$HI_i = EC_{nRi} - EC_{nFi} \quad (1)$$

148 Where EC_{nRi} and EC_{nFi} are normalized EC values at discharge interval i, taken on the
149 rising limb and falling limb of the loop, respectively. Figure 2 represents local HI_i values and the
150 slope value for an illustrative storm event. The mean of the 19 HI_i values (5% intervals,
151 recommended by Lloyd et al, 2016) is used as the final HI value. As a result, HI values range
152 from -1 to 1, absolute values near 0 and 1 corresponding to low and high hysteresis degrees,
153 respectively (similar versus contrasting rising and falling paths). Negative HI values indicate
154 anticlockwise loops whereas positive HI values indicate clockwise loops. Complex 8-shaped
155 loops show an HI value corresponding to their primary shape (i.e. the widest loop part with one
156 rotational direction).
157
158 [Figure 2]
159

Once threshold values are defined (values of slope and HI that delineate the classification types), measure slope and HI make it possible to relate any storm event to one of the nine categories of the classification presented in Figure 3, using its C-Q loop. The loop typology is built on two-character names, the first corresponding to HI sign (and consequently to rotational direction: C for clockwise, N for neutral and A for anticlockwise), and the second corresponding to the slope sign (- for negative s, 0 for nil s, and + for positive s). This classification based on Butturini et al. (2008) was adapted to the case of EC-Q in karst catchments.

In the case of karst areas, event water (EW) having a lower residence time than pre-event water (PEW), its EC value is lower. Indeed, EC is a reliable proxy of bicarbonates concentration, which is linked to limestone dissolution and thus residence time (Peyraube et al., 2019). Therefore, we will use our EC-Q loop typology to determine patterns of successive contributions to streamflow (PEW and EW), assuming the EC ranking is known.

Each loop type is linked to a specific pattern of successive contributions to streamflow, based on the main findings in the literature of C-Q studies. Evans and Davies (1998) showed that, in a two-component system, when the solute concentration of PEW is higher than that of EW, anticlockwise C-Q loops indicate a dominant contribution of EW during the rising limb, and a dominant contribution of PEW during the falling limb (scenario 1). On the other hand, clockwise C-Q loops indicate a dominant PEW contribution during the rising limb and a dominant EW contribution during the falling limb (scenario 2). This C-Q loop taxonomic consistency was verified experimentally by Chanat et al. (2002), and was shown to be reliable when concentration values of end-members are distinct enough, which is the case here as surface

runoff water and groundwater are compared (see values at end of section 3.3). Regarding the specific case of EC-Q hysteresis, Toran and Reisch (2012) observed anticlockwise loops during storm events at a karst spring discharge in Pennsylvania and verified that they were linked to Scenario 1 based on Ca^{2+} and Mg^{2+} concentration monitoring. Rose et al. (2018) linked Scenario 2 to clockwise C-Q loops thanks to geogenic solute monitoring in a small USA catchment. In the case of monitoring of solutes in which EW is enriched, such as NO_3^- from the organic horizon (Evans et al., 1999; Huebsch et al., 2014), the rotational directions are reversed.

Based on previously described findings from the literature and in our case of EC monitoring in a karst catchment where the PEW solute concentration is higher, our hypothesis is that clockwise EC-Q loops correspond to PEW preceding EW and anticlockwise EC-Q loops correspond to EW preceding PEW. This is particularly clear with loops that have slopes equal to zero (C0 and A0 loops), rising and falling limbs showing EC values exclusively above or below the initial value prior to a storm event. In the case of non-zero loop slopes, one limb may have mixed water origins. A mixed water signature, in the case of karst systems where fast infiltration can occur, may result from low residence time PEW recently stored in the karst (i.e., from several days or weeks) or from EW infiltrating through preferential pathways and mixing with highly mineralized PEW (i.e. several months or years old). Regarding non-hysteretic EC-Q paths, both limbs have a similar water origin, this latter being inferred from the slope (a negative slope indicating EW contribution whereas a positive slope indicating PEW contribution).

This methodology is applicable only when the initial EC value falls between the two end-member EC values. This observation was systematically verified in the framework of this study (the initial EC value always being higher than the EW end-member EC value in karst areas). More information on end-member EC values is provided in section 3.3. On Figure 3 that presents

205 the nine loop types of our classification, a framework of interpretation of associated streamflow
206 contribution patterns is also proposed based on residence time, which is inferred from EC values.
207 Mixed water can be linked either to a mix of low and high residence time PEW or to a mix of
208 EW and high residence time PEW.
209
210 [Figure 3]
211

212 ## *2.3 Reach-scale approach: lateral flow simulation*

213 To investigate the origin of lateral inflows along river reaches (i.e. between two gauging
214 stations), we used the modeling approach proposed by Cholet et al. (2017) based on the diffusive
215 wave equation (DWE) and extended to the advection–diffusion equation (ADE). Both equations
216 are resolved using the Hayami analytical solution (1951) as proposed by Moussa (1996). We
217 provide in this section the key points of the approach. More details on this analytical approach
218 are provided in the Appendix.
219 Separate modeling of lateral discharge Q_L and mass flux M_L make it possible to assess
220 lateral solute concentration C_L by division, as shown in equation 2.

221 $$C_L = \frac{M_L}{Q_L} \quad (2)$$

222 Q_L is simulated using the solution of the inverse problem of the DWE and ADE,
223 assuming that lateral flow is uniformly distributed along the river reach (Moussa, 1996). M_L is
224 obtained by applying the DWE to mass flux, this latter being calculated as the product of Q_L and
225 C_L (equation 2). Assuming that total dissolved solids (TDS) consists mainly of conductive ionic
226 compounds, EC is proportional to the TDS concentration (noted C, in $g.m^{-3}$). Concentration C is

therefore calculated from EC, using a constant factor of 0.64, in accordance with values found in the literature (Lloyd and Heathcote, 1985):

$$C = EC \cdot 0.64 \quad (3)$$

Mass flux M is then calculated as the product of concentration C and discharge Q:

$$M = C \cdot Q \quad (4)$$

Finally, the simulated lateral conductivity EC_L is calculated as the ratio of simulated lateral mass flux M_L to simulated lateral discharge Q_L, divided by a factor of 0.64:

$$EC_L = \frac{M_L}{Q_L} \cdot \frac{1}{0.64} \quad (5)$$

As some river reaches can show negative Q_L values, indicating lateral streamflow losses, EC_L is calculated only for positive Q_L values. Indeed, negative Q_L values would lead to negative EC_L values, which is impossible. EC_L variations thus make it possible to compare water origin on successive streams within a catchment.

3 Study areas and data sets

3.1 Study areas

The previously described methodology was applied to two catchments in France, which are partially to strongly karstified, and located in different geological and hydrometeorological settings (figure 4). They are similar in size (~ 1000 km²) and both include four Q and EC measurement stations.

The Loue River basin is located in the Jura Mountains. Its outcrops consist primarily of extensively and homogeneously karstified Jurassic limestone and locally marl, making it a unary

248 karst basin. The Lison River is the major left bank Loue tributary and oth rivers start as a karst
249 spring. The Loue spring being partly fed by Doubs river losses that occur in the southeastern part
250 of the catchment (Charlier et al., 2014), it is not a typically unary karst basin. The term of unary
251 karst basin is used here as the allogenic recharge is also from a similar karstified area. The Loue
252 and Lison springs are among the largest karst springs in Europe (Chen et al., 2017), with mean
253 discharge of around 10 and 7 $m^3.s^{-1}$, respectively, and maximum peak flows of around 80 and 70
254 $m^3.s^{-1}$. Precipitation follows an elevation gradient; annual values range from 1600 mm on the
255 upstream catchment at elevations of 900 m (a.s.l) to 1450 mm at the outlet, at an elevation of
256 around 400 m (a.s.l).
257 The Cèze catchment is located in the eastern part of the Cévennes Mountains. It can be
258 characterized as a binary karst basin with upstream areas that consist of non-karst outcrops (i.e.
259 hard rocks) where mean yearly precipitation is 1500 mm and median and downstream areas
260 underlain by karst plateaus that receive precipitation of approximately 1000 mm/year. The
261 karstified portion is composed of early Cretaceous limestone (dark green, figure 54b) that is
262 mainly situated between the Tharaux and Laroque stations, and extends southward. More
263 information on exchanges between river streams and karst systems in this area can be found in
264 the work of Chapuis (2018).
265
266 [Figure 4]
267

3.2 Data sets

Detailed information on the data time series is available in the supplementary material. Temporal data used in this paper are:

- Hourly streamflow data, available from the French public streamflow database 'Banque Hydro' (http://www.hydro.eaufrance.fr).
- Hourly rainfall data, available from the Antilope database (Champeaux et al., 2011), a reanalysis produced by the French public meteorological service Météo France (http://www.meteofrance.fr/).
- Sub-hourly EC measurements for the Cèze river, recorded by the BRGM using Schlumberger CTD diver probes from July 2019 to July 2020. Similar data recorded using OTT MS5 probes within the QUARSTIC network (Charlier et al., 2018) for the Loue River, from January 2016 to January 2020.

As available data time series on the studied catchments are not of identical length and because of contrasted hydro-climatic contexts, 58 storm events were extracted for the Loue catchment, against 8 for the Cèze catchment. In the Loue catchment, storm events have a median precipitation depth of 58 mm (min: 10 mm and max: 136 mm) and a median peak flow value of 78 $m^3.s^{-1}$ (min: 2 $m^3.s^{-1}$ and max: 529 $m^3.s^{-1}$). In the Cèze catchment, storm events have a median precipitation depth of 65 mm (min: 30 mm and max: 180 mm) and a median peak flow value of 128 $m^3.s^{-1}$ (min: 20 $m^3.s^{-1}$ and max: 780 $m^3.s^{-1}$).

3.3 EC end-member values

For the Loue catchment, the PEW end-member EC is defined as the signal for water having the longest residence time, thus having the highest EC value (at 550 $\mu S.cm^{-1}$) recorded during the acquisition period at the spring monitoring stations (Ouhans and Nans, see figure 4a). The Loue catchment EW end-member EC for surface runoff is defined at 250 $\mu S.cm^{-1}$, based on values recorded on an intermittent stream on marly areas. For the Cèze catchment, the PEW end-member is defined at 700 $\mu S.cm^{-1}$, based on highest values recorded at Cèze karst springs monitoring stations (Chapuis, 2018). The Cèze catchment EW end-member EC for surface runoff is defined at 75 $\mu S.cm^{-1}$, based on minimum values recorded during the acquisition period at the upstream monitoring station (Tharaux, see figure 4b) which is only fed by non-karst areas.

4 Results

4.1 EC-Q relationships at the catchment scale

Figure 5 compares annual and event-based mean EC values for the Loue and Cèze catchment stations. To obtain the mean EC value of all water flowing through stations, we calculated the flow-weighted average of hourly EC..

For both annual and event-based EC, the four Loue stations show similar values, of around 400 and 350 $\mu S.cm^{-1}$, respectively. This consistency across stations is probably linked to the homogeneous presence of karst areas, leading to similar proportions of surface water and groundwater contribution to streamflow. Event-based EC values are generally higher than annual

309 ones, indicating a dominant mobilization of pre-event highly mineralized water during storms,
310 likely groundwater, as the two downstream river stations (Vuillafans and Chenecey) show
311 similar responses to the two spring stations (Nans and Ouhans).

312 The Cèze catchment stations show a spatial variability pattern, with EC values increasing
313 from upstream to downstream and decreasing again at the most downstream station. Annual
314 values range from 180 $\mu S.cm^{-1}$ at Tharaux to 280 $\mu S.cm^{-1}$ at Laroque. Event-based EC values
315 follow the same trend, in relation to the local karst extension: the intermediate karst area located
316 between Tharaux and Laroque (see fig 5b) promoting highly mineralized water. Event-based EC
317 values are mostly lower than annual ones, showing a dominant stream dilution by low-
318 mineralization event water during storms, except at the Tharaux station.
319
320 [Figure 5]
321
322 Figure 6 shows two examples of recorded EC and Q variations for each study site (Loue:
323 a,b; Cèze: c,d), along with their corresponding EC-Q loops (see Figure 3 for classification).
324 These illustrative events were chosen as they are representative of the generally observed EC and
325 Q variations at each site. Regarding the Loue catchment, figure 6a shows a storm event
326 associated with an EC drop that takes place mostly after peak flow and leads to a C- loop type
327 indicating an event-water (EW) contribution that occurs mainly at the end of peak flow and
328 during recession. Figure 6b shows that other storm events on the Loue catchment are associated
329 with an EC increase, indicating pre-event water (PEW) mobilization. On the pictured storm-
330 event, EC variations are quite similar to Q variations, leading to a flatter EC-Q loop.

331 Nevertheless, EC values are slightly higher on the falling limb, leading to an identifiable A+ loop
332 type.
333 Regarding the Cèze catchment, figure 6c illustrates a storm event associated with an EC
334 decrease, indicating dilution by event water and leading to a C- loop type, as shown in figure 6a.
335 Finally, figure 6d represents a storm event with strongly anticorrelated EC and Q variations
336 during both rising and falling limbs, leading to a non-hysteretic N- loop type.
337
338 [Figure 6]
339
340 Figure 7a and 7b show the seasonal slope value distribution in the Loue and Cèze
341 catchments, respectively. All stations in the Loue catchment exhibit a similar pattern of seasonal
342 variation, with negative or low slopes in winter (November to March) and spring (April to May),
343 and positive values in summer (June to August) and fall (September to October). This shows that
344 storm events in winter and spring are primarily characterized by an EW dilution while storm
345 events in summer and fall are mainly characterized by a PEW mobilization. From June to
346 October, the variability of slope is higher. Moreover, slope values are generally lower at the
347 Nans and Chenecey stations than at the others.
348 Regarding the Cèze catchments, slope values are mostly negative all year long, except for
349 a few winter storm events at the Tharaux and Bagnols stations, indicating the dominant dilution
350 by low-mineralization EW.
351 Figures 7c and 7d show the HI value distribution following seasons for the Loue and
352 Cèze catchments, respectively. Both catchments are subject to strong seasonal influence, even
353 though the patterns are different. The Loue catchment stations show mostly positive HI values in

354 winter and spring, and negative HI values in summer and fall. This corresponds to clockwise and
355 anticlockwise EC-Q loops, respectively. Analyzed in line with slope values (see Figure 3), these
356 loops show that in winter and spring, the dominant contribution is EW, with a minor contribution
357 of PEW at the beginning of storm events. In summer and fall, the dominant contribution is PEW,
358 with a minor contribution of EW or slightly mineralized PEW at the beginning of storm events.
359 Contrary to the Loue catchment, Cèze catchment stations show mostly positive HI values
360 in fall, corresponding to clockwise loops. During this season, slope values are mostly negative,
361 showing that the dominant contribution is EW, associated with a minor contribution of PEW at
362 the beginning of storm events. In winter, HI values are near zero, corresponding to non-
363 hysteretic EC-Q paths (similar EC values for a given discharge amount on rising and falling
364 limbs). During this season, slope values are primarily negative, showing that the dominant
365 contribution is EW on both limbs.
366
367 [Figure 7]
368
369 Table 1 summarizes the main EC-Q loop types on the Loue and Cèze catchments for all
370 seasons. In the Loue catchment, predominantly clockwise EC-Q hysteresis loops (C- and C0)
371 occur during winter and spring, while anticlockwise loops (A0 and A+) dominate in summer and
372 fall. Conversely, the Cèze catchment stations show mostly non-hysteretic behavior in winter (N-
373 loops) and show clockwise loops (C- and C0) in summer and fall.
374
375
376

377 *Table 1: Commonly occurring EC-Q loop types on the Loue and Cèze catchments*

Catchment	Station	Sep-Oct	Nov-Mar	Apr-May	Jun-Aug
Loue	Nans	A+	C-	C-	N0
	Ouhans	A+	C-	C+	N+
	Vuillafans	A+	C0	C+	A+
	Chenecey	A0/A+	C0	N0	A+
Cèze	Tharaux	C-	N-	-	C+
	Montclus	~	N-	-	C0
	Laroque	C-	N-	-	C-
	Bagnols	C0	~	-	C-

378 - = no storm event and ~ = no clear dominant behavior

379

380 As these results provide information for nested catchments, their analysis on successive
381 stations can highlight spatial variability in flood water origin towards the final outlet. Even
382 though EC-Q loop types are quite homogeneous for the four stations for a given catchment, some
383 differences are observed. Regarding Loue catchment, the Nans and Chenecey stations have
384 particularly low slope values. Indeed, except for summer events, most of their EC-Q loops have
385 slopes lower than 1 (figure 7a). This indicates a greater EW effect at the Nans-Chenecey and
386 Vuillafans-Chenecey (downstream reaches, see figure 4a). This is also the case regarding Cèze
387 catchment, where lower slopes are characterized for Montclus. Because each nested catchment
388 incorporates the upstream previous one, these intra-site trends are not totally straightforward and
389 can hardly be quantified.

390

391 ## *4.2 EC of reach-scale lateral flow*

392 Figure 8 shows examples of observed Q and EC at input (Q_{IN}) and output (Q_{OUT}) stations,
393 as well as simulated lateral Q_L and EC_L for the Loue (a, b) and Cèze (c, d) catchments. On the

394 Loue catchment example (left), EC_L, EC_{IN}, and EC_{OUT} are similar with values ranging between
395 350 and 400 µS.cm^{-1}, meaning that the mass flux remains quite proportional to discharge rate.
396 On the Cèze catchment example (right), as Q_O is slightly delayed near peak flow, simulated Q_L
397 shows a brief period of loss (negative values). The corresponding EC_L is not calculated for
398 outflows, as it would lead to negative values. EC_L for inflows values are around 250 µS.cm-1,
399 slightly higher than measured input and output EC (200 µS.cm-1), indicating PEW mobilization.
400 EC_L values decrease at the end of the period, indicating the decreased contribution of PEW.
401
402 [Figure 8]
403
404 Figure 9 shows the distribution of simulated lateral flow EC on the Loue and Cèze River
405 reaches. EC_L mean values are calculated around the peak of lateral flow ($Q_L > 0.75Q_{L,max}$), so as
406 to obtain a value that is representative of the major amount of lateral water inflow. Values of EW
407 and PEW EC end members are also plotted on the graphs. As the simulation of EC_L values is
408 made using the DWE, it requires a simple reach with one input and one output. For this reason,
409 the Nans-Chenecey reach is not represented (see the river confluence on figure 4a).
410 Regarding the Loue catchment (figure 9a), the upstream reach (Ouhans-Vuillafans)
411 shows EC_L values mainly above 400 µS.cm^{-1}, except for some winter storm events. Lateral water
412 inflows are thus of mixed origin. On the downstream reach (Vuillafans-Chenecey), EC_L values
413 are lower, mostly less than 400 µS.cm^{-1}. This reach-scale approach provides more precise and
414 discretized information of the streamflow contribution variability within catchment, and is
415 consistent with the lower slope values measured at the Chenecey station in figure 7, indicating a
416 higher EW signature. This can be explained by a higher contribution of either surface runoff

downstream the canyon area (open valleys in the downstream parts of the catchment) or EW from fast infiltration pathways, or both. It is also noticeable that EC_L distribution are more spreaded on the downstream reach, probably due to more intense or frequent water mixing.

On the Cèze catchment (figure 9b), EC_L values span from 100 to 300 $\mu S.cm^{-1}$ on the two median reaches (Tharaux-Montclus and Montclus-Laroque), whereas most EC_L values on the downstream reach (Laroque-Bagnols) are lower (around 100 $\mu S.cm^{-1}$). This pattern is consistent with its karst outcrop location, located between Tharaux and Laroque (figure 4b) and the EC river measurement (figure 5b).

[Figure 9]

5 Discussion

5.1 Conceptual model of flood water origin and process variability

Figures 10a to 10d show the main hysteresis loop types, associated hydrographs, and the scheme of flood water origin and processes for the Loue (unary) and Cèze (binary) karst catchments, for two contrasted periods in the hydrological cycle. Figures 10e and 10f represent, within each catchment, the reach-scale variability of streamflow contribution. The conceptual model provides key insights into the influence of seasons and karst configuration on flood processes.

437 In the Loue unary karst catchment, mainly C- type EC-Q loops are observed from
438 November to May (figure 10a), corresponding to a dominant contribution sequence of 1) mix of
439 EW and PEW and 2) EW. This sequence can be explained by a two-step process involving 1)
440 during the rising limb, EW infiltrating into karst drains and pushing PEW into the stream,
441 associated with EW from fast infiltration or surface runoff, and 2) during the falling limb, EW
442 that infiltrated into karst drains reaching the stream, associated with surface runoff. From June to
443 October (figure 10b), mainly A+ type loops are observed, corresponding to a dominant
444 contribution sequence of 1) mixed water and 2) PEW. This can be explained by a lower degree
445 of saturation in the karst system, reducing surface runoff contribution, and showing a purely
446 piston-type flow leaching the PEW initially stored in the aquifer.
447 In the Cèze binary karst catchment N- type loops are the most common between
448 November and May (figure 10c), corresponding to a dominant contribution of EW during both
449 rising and falling limbs. This pattern is explained by the lower storage capacity of smaller karst
450 units compared to the Loue catchment. The high karst system saturation level leads to a blocked
451 infiltration and promotes increased EW surface runoff. From June to October (figure 10d), C-
452 EC-Q loops are the most common type observed, corresponding to a dominant contribution
453 sequence of 1) mixed water and 2) EW. At this period of the year, the karst system is less
454 saturated, which reduces the surface runoff signature associated with blocked infiltration, and
455 shows PEW reaching streams by piston-type flow, associated with the EW influence, leading to
456 similar processes as described for figure 10a.
457
458 [Figure 10]
459

460 The surface runoff contribution to streamflow is less important in the Loue catchment
461 compared to the Cèze one, as seen in previous sections. This fact is explained by the catchment's
462 morphology, which is for the unary catchment a typical configuration of plateaus and canyons
463 that promotes higher rainfall infiltration and groundwater contribution to surface flows (Le
464 Mesnil et al., 2020). This type of surface water-groundwater interaction is promoted in other
465 catchments made up of plateaus and canyons, where stream losses and/or lateral gains from
466 springs occur according to hydrological conditions (Bailly-Comte et al., 2009; De Waele, 2010;
467 Charlier et al., 2019). Our results confirm this behavior, which results in increased EC values and
468 positive slope values of the hysteresis EC-Q loops. Because the saturation level of the karst
469 aquifer also plays an important role on the mobilisation of PEW and EW, its low or high storage
470 capacity can affect flood process variability. To interpret surface runoff contributions in the Cèze
471 catchment, we need to refer to the two main types of flooding that are documented in the
472 literature for karst areas: 1) infiltration excess runoff due to the low infiltration capacity of the
473 karst medium (Maréchal et al. 2008), and 2) backflooding following infiltration with a
474 simultaneous rapid rise of the aquifer water level due to a limited saturation capacity of the
475 conduit network (Lopez-Chicano et al. 2002; Bonacci et al. 2006; Bailly-Comte et al. 2008). The
476 first process is linked to rainfall intensities, that are high under the specific Mediterranean
477 climate of the Cèze river. The second one is more dependent on the storage capacity of the karst
478 aquifer, which is small for the Cèze (compared to high elevation plateaux for the Loue).
479 Superimposed on seasonal influence, physiographical factors also control intra-site
480 variability of flood processes and catchment's response to storm events. Indeed, the extension of
481 karst areas and topographic relief can both affect the water origin of streamflow. In the Loue
482 catchment, the reach-scale lateral flow simulation (section 4.2) highlights a water origin spatial

variability characterized by an increasing EW contribution to storm events in the downstream direction. This increased EW contribution is explained by the typical plateau-and-canyon morphology of the upstream portion grading into open valleys downstream, resulting in higher surface runoff.

The Cèze catchment, as shown in figure 4b, is characterized by a binary karst, that is, a delineated karstified area downstream of hard-rock headwater zones. Le Mesnil et al. (2020; 2021) showed that this specific karst location plays a role in the annual water budget, as well as in the flood pattern. In this study, EC monitoring shows that it also controls flood water origin, as illustrated by EC values increasing on the karst zone (figure 5b). This spatial variability within the Cèze catchment was detected by our reach-scale approach of lateral flow simulation, EC_L values being increasing in the median reaches where the karst crops out. This approach shows that water being mobilized during floods has a higher PEW signature in this zone. Figures 10e and 10f provide a sketch of the main features of streamflow contribution variability within each study site.

5.2 Pros and cons of the C-Q relationship analysis approach

Our approach makes it possible to differentiate storm events in which PEW may or may not be mobilized, thanks to EC monitoring. This approach is a suitable for assessing the role of groundwater in flooding, which in many cases is supposed to be mobilized without being quantified (e.g. Ascott et al., 2017). For example, applying this methodology in the context of groundwater-induced flooding in chalk regions (Finch et al., 2004; Pinault et al., 2005) or lowland karst areas (Jerome Morrissey et al., 2020) may be of great value, as well as for rivers that show complex and variable exchanges with underlying aquifers (Bailly-Comte et al., 2009;

505 Charlier at al., 2015; 2019). Indeed, a better understanding of the groundwater role in flooding is
506 essential for efficient management of flood hazards in karst areas. Several authors develop tools
507 in this purpose (Gill et al., 2013; Mayaud et al., 2019). A recent study of Le Mesnil et al. (2021)
508 based on 108 gauging stations shows in the one hand that karst promotes generally peak-flow
509 attenuation due partly to higher water infiltration from rivers, and in the other hand that the
510 hydrological response is highly site-specific. The development of approaches investigating water
511 origin as proposed in this paper gives interesting perspective to explore such variability and to
512 facilitate their modeling, for example using semi-distributed models. Moreover, the proposed
513 approach was kept generic enough to be applicable to a variety of contexts. This section provides
514 a brief summary of the main features of this two-step methodology, what can be expected from
515 its application, and what it requires.

516 The nested-catchment scale approach is integrative, as it provides information on the
517 topographic catchment from a particular monitoring station to its upstream limit. Even so,
518 analysis of results at successive monitoring stations provides information on water origin and
519 flood process variability along the river. Loop slope and hysteresis index (Lloyd et al., 2016) of
520 C-Q paths can be used to classify storm events through the use of a loop typology adapted and
521 enriched from the work of Evans and Davies (1998). Other hysteresis classifications have been
522 proposed previously for karst areas, but include less types and do not allow to represent all storm
523 processes: e.g. the 3-type T-C curve classification by Fournier et al. (2007). Our classification
524 can be used with a variety of parameters (EC, concentrations, turbidity, …) involving different
525 processes. In the framework of this study, it allowed determining flood water origin seasonal
526 patterns on the two studied catchments. This first approach requires only concentration and
527 discharge datasets at a consistent resolution (hourly for storm-event analysis, possibly wider time

528 steps for other purposes) for one outlet station. It can thus be easily implemented at little cost
529 (especially for EC continuous monitoring).
530 This nested-catchment scale approach involves some limitations. First, the concentration
531 ranking of potential contributing end-members must be known to make a consistent
532 interpretation of the involved processes. Then, no more than two end members can be
533 differentiated when monitoring one concentration variable. Finally, in the specific case of karst
534 systems, the approach cannot always properly differentiate between EW that originates from
535 surface runoff and EW that originates from fast infiltration through underground karst conduits.
536 Indeed, localized infiltration in sinkholes for instance can be quick enough to keep water
537 chemistry unchanged due to residence times of few hours/days. In this case, other techniques
538 such as signal processing or baseflow separation might be necessary to figure out
539 comprehensively which flood processes are involved, as well as analysis of alternative physico-
540 chemical data such as organic carbon to track infiltration water with short residence time (Pronk
541 et al., 2009; Charlier et al., 2012). Some anomalous EC variations can also be witnessed during
542 high-flow periods, as groundwater catchments expand and incorporate areas of different typical
543 EC values (Ravbar et al., 2011).
544 The reach-scale approach is based on the inverse modeling approach (Moussa, 1996)
545 using the diffusive wave equation. It allows simulating Q and C variations in lateral exchange
546 flow of a river reach (Cholet et al., 2017). Analyzed along with end-member EC values, this
547 analysis highlighted the increasing contribution of EW towards the downstream end of the Loue
548 catchment and the major PEW contribution in the karst zone in the median area of the Cèze
549 catchment. This analytical approach is very convenient as it allows investigating spatial

variability of lateral exchanges without conducting extensive field work such as tracing tests (e.g. Covino et al., 2011).

This second part is more data-dependent, as it requires similar datasets than the first part, but recorded at both inlet and outlet stations. Moreover, the approximate EC value of each end member must be known to interpret the results in terms of water origin mixing. Though, this reach-scale approach provides more precise and discretized information on spatial variability of streamflow contributions within catchments.

6 Conclusions

We applied a C-Q relationship analysis approach, using hysteresis loop classification at the nested catchment scale combined with lateral flow and concentration simulation at the reach scale. In the framework of this study, this combined method made it possible to establish a seasonal conceptual model of water origin during storm events for two contrasted karst catchments and to infer its spatial variability at the scale of the monitoring network.

Analysis of EC-Q hysteresis loops highlighted a flood water origin pattern, with successive contributions of pre-event water (PEW) and event water (EW) according to karst type (unary vs. binary) and seasonality (low flow periods vs. high flow periods). Simulation of lateral exchange flows led to a more detailed analysis of the water origin, spatializing it at the reach scale. This analysis highlighted the decreasing contribution of PEW in favor of EW as the canyons and plateaus that the Loue flows through grade into open valleys, the significant PEW effect on the karst area of the Cèze catchment, and the role of the aquifer saturation state in flood response.

Our results show that, in karst context the nested catchment scale analysis of C-Q hysteresis loops provides information on seasonality of flood processes, and trends of intra-catchment variability. We also show that the reach scale lateral flow simulation provides a quantifiable information on intra-catchment variability of streamflow contributions. The tested approach is innovative and particularly suitable for partly karstified catchments, as it is semi-distributed and uses EC measurements which are a reliable proxy of water residence time. Our results are encouraging to apply these complementary methodologies to a variety of sites of differing geology, with additional investigational purposes, such as water resource management and modeling. Indeed, such approach providing discretized information on flood processes within catchments could help refining lumped model structure, or facilitate the use of semi-distributed models. Some perspectives are identified, as coupling the monitoring of multiple solutes, making it possible to differentiate additional end members.

Author contribution

RM and JBC were involved in conceptualization, funding acquisition, and supervision. MLM gathered the data and designed the methodology with the help of JBC, RM, and YC. MLM prepared the manuscript with the help of all co-authors.

Acknowledgments

The work was funded by the French Governmental Administration for Risk Prevention (DGPR), the Service Central d'Hydrométéorologie et d'Appui à la Prévision des Inondations (SCHAPI), and the French Geological Survey (BRGM).

Hourly streamflow data were gathered from the “Banque hydro” database using a script available at http://doi.org/10.5281/zenodo.3744183. EC datasets of the Loue catchment were monitored within the QUARSTIC network funded by the BRGM, the Doubs Department, and the Rhône Mediterranean Corsica Water Agency, and the NUTRI-Karst project founded by BRGM and Rhône Mediterranean Corsica water agency.

The authors declare that they have no known competing financial interests or personal relationships that could have appeared to influence the work reported in this paper.

References

Anderson, S. P., Dietrich, W. E., Torres, R., Montgomery, D. R., & Loague, K. (1997). Concentration-discharge relationships in runoff from a steep, unchanneled catchment. Water Resources Research, 33(1), 211–225. https://doi.org/10.1029/96WR02715

Ascott, M. J., Marchant, B. P., Macdonald, D., McKenzie, A. A., & Bloomfield, J. P. (2017). Improved understanding of spatio-temporal controls on regional scale groundwater flooding using hydrograph analysis and impulse response functions. Hydrological Processes, 31(25), 4586–4599. https://doi.org/10.1002/hyp.11380

Baeumer, B., Benson, D. A., Meerschaert, M. M., & Wheatcraft, S. W. (2001). Subordinated advection-dispersion equation for contaminant transport. Water Resources Research, 37(6), 1543–1550. https://doi.org/10.1029/2000WR900409

Bailly-Comte, V., Jourde, H., Roesch, A., Pistre, S., & Batiot-Guilhe, C. (2008). Time series analyses for Karst/River interactions assessment: Case of the Coulazou river (southern France). Journal of Hydrology, 349(1–2), 98–114. https://doi.org/10.1016/j.jhydrol.2007.10.028

614 Bailly-Comte, V., Jourde, H., & Pistre, S. (2009). Conceptualization and classification of
615 groundwater–surface water hydrodynamic interactions in karst watersheds: Case of the karst
616 watershed of the Coulazou River (Southern France). Journal of Hydrology, 376(3–4), 456–462.
617 https://doi.org/10.1016/j.jhydrol.2009.07.053
618 Bakalowicz, M. (2005). Karst groundwater: a challenge for new resources. Hydrogeology
619 Journal, 13(1), 148–160. https://doi.org/10.1007/s10040-004-0402-9
620 Bonacci, O., Ljubenkov, I., & Roje-Bonacci, T. (2006). Karst flash floods: an example
621 from the Dinaric karst (Croatia). Natural Hazards and Earth System Science, 6(2), 195–203.
622 Burns, D. A., McDonnell, J. J., Hooper, R. P., Peters, N. E., Freer, J. E., Kendall, C., &
623 Beven, K. (2001). Quantifying contributions to storm runoff through end-member mixing
624 analysis and hydrologic measurements at the Panola Mountain Research Watershed (Georgia,
625 USA). Hydrological Processes, 15(10), 1903–1924. https://doi.org/10.1002/hyp.246
626 Butturini, A., Alvarez, M., Bernal, S., Vazquez, E., & Sabater, F. (2008). Diversity and
627 temporal sequences of forms of DOC and NO3-discharge responses in an intermittent stream:
628 Predictable or random succession?. Journal of Geophysical Research: Biogeosciences, 113(G3).
629 Champeaux, J.-L., Laurantin, O., Mercier, B., Mounier, F., Lassegues, P., & Tabary, P.
630 (2011). Quantitative precipitation estimations using rain gauges and radar networks: inventory
631 and prospects at Meteo-France, 11.
632 Chanat, J. G., Rice, K. C., & Hornberger, G. M. (2002). Consistency of patterns in
633 concentration-discharge plots. Water Resources Research, 38(8), 22-1-22–10.
634 https://doi.org/10.1029/2001WR000971
635 Chapuis, H. (2018). Caractérisation, évaluation, modélisation des échanges entre
636 aquifères karstiques et rivières - Application à la Cèze (Gard, France), 467.

637 Charlier, J.-B., Bertrand, C., & Mudry, J. (2012). Conceptual hydrogeological model of
638 flow and transport of dissolved organic carbon in a small Jura karst system. Journal of
639 Hydrology, 460–461, 52–64. https://doi.org/10.1016/j.jhydrol.2012.06.043
640 Charlier J.-B., Desprats J.-F., Ladouche B. (2014). Appui au SCHAPI 2014 – Module 1 –
641 Rôle et contribution des eaux souterraines d'origine karstique dans les crues de la Loue à
642 Chenecey-Buillon, BRGM/RP-63844-FR report, 109p. https://infoterre.brgm.fr/rapports/RP-
643 63844-FR.pdf (accessed February 2021)
644 Charlier, J.-B., Moussa, R., Bailly-Comte, V., Danneville, L., Desprats, J.-F., Ladouche,
645 B., & Marchandise, A. (2015). Use of a flood-routing model to assess lateral flows in a karstic
646 stream: implications to the hydrogeological functioning of the Grands Causses area (Tarn River,
647 Southern France). Environmental Earth Sciences, 74(12), 7605–7616.
648 https://doi.org/10.1007/s12665-015-4704-0
649 Charlier J.-B., Vallet A., G. Hévin, F. Moiroux (2018) – Projet QUARSTIC : QUAlité
650 des eaux et Réseau de Surveillance des rIvières Comtoises. BRGM/RP-68315-FR report, 165p.
651 http://infoterre.brgm.fr/rapports/RP-68315-FR.pdf (accessed February 2021)
652 Charlier, J., Moussa, R., David, P., & Desprats, J. (2019). Quantifying peakflow
653 attenuation/amplification in a karst river using the diffusive wave model with lateral flow.
654 Hydrological Processes. https://doi.org/10.1002/hyp.13472
655 Chen, Z., Auler, A. S., Bakalowicz, M., Drew, D., Griger, F., Hartmann, J., et al. (2017).
656 The World Karst Aquifer Mapping project: concept, mapping procedure and map of Europe.
657 Hydrogeology Journal, 25(3), 771–785. https://doi.org/10.1007/s10040-016-1519-3
658 Cholet, C., Charlier, J.-B., Moussa, R., Steinmann, M., & Denimal, S. (2017). Assessing
659 lateral flows and solute transport during floods in a conduit-flow-dominated karst system using

660 the inverse problem for the advection–diffusion equation. Hydrology and Earth System Sciences,
661 21(7), 3635–3653. https://doi.org/10.5194/hess-21-3635-2017
662 Cimorelli, L., Cozzolino, L., Della Morte, R., & Pianese, D. (2014). Analytical solutions
663 of the linearized parabolic wave accounting for downstream boundary condition and uniform
664 lateral inflows. Advances in Water Resources, 63, 57–76.
665 https://doi.org/10.1016/j.advwatres.2013.11.003
666 Covino, T., McGlynn, B., & Mallard, J. (2011). Stream-groundwater exchange and
667 hydrologic turnover at the network scale. Water Resources Research, 47(12).
668 https://doi.org/10.1029/2011WR010942
669 De Waele, J., Martina, M. L. V., Sanna, L., Cabras, S., & Cossu, Q. A. (2010). Flash
670 flood hydrology in karstic terrain: Flumineddu Canyon, central-east Sardinia. Geomorphology,
671 120(3–4), 162–173. https://doi.org/10.1016/j.geomorph.2010.03.021
672 Doctor, D. H., Alexander, E. C., Petrič, M., Kogovšek, J., Urbanc, J., Lojen, S., &
673 Stichler, W. (2006). Quantification of karst aquifer discharge components during storm events
674 through end-member mixing analysis using natural chemistry and stable isotopes as tracers.
675 Hydrogeology Journal, 14(7), 1171–1191. https://doi.org/10.1007/s10040-006-0031-6
676 Evans, C., Davies, T. D., & Murdoch, P. S. (1999). Component flow processes at four
677 streams in the Catskill Mountains, New York, analysed using episodic concentration/discharge
678 relationships. Hydrological Processes, 13(4), 563–575. https://doi.org/10.1002/(SICI)1099-
679 1085(199903)13:4<563::AID-HYP711>3.0.CO;2-N
680 Evans, Christopher, & Davies, T. D. (1998). Causes of concentration/discharge hysteresis
681 and its potential as a tool for analysis of episode hydrochemistry. Water Resources Research,
682 34(1), 129–137. https://doi.org/10.1029/97WR01881

683 Finch, J. W., Bradford, R. B., & Hudson, J. A. (2004). The spatial distribution of
684 groundwater flooding in a chalk catchment in southern England. Hydrological Processes, 18(5),
685 959–971. https://doi.org/10.1002/hyp.1340
686 Fournier, M., Massei, N., Bakalowicz, M., Dussart-Baptista, L., Rodet, J., & Dupont, J. P.
687 (2007). Using turbidity dynamics and geochemical variability as a tool for understanding the
688 behavior and vulnerability of a karst aquifer. Hydrogeology Journal, 15(4), 689–704.
689 https://doi.org/10.1007/s10040-006-0116-2
690 Gill, L. W., Naughton, O., & Johnston, P. M. (2013). Modeling a network of turloughs in
691 lowland karst: Modeling a Network of Turloughs in Lowland Karst. Water Resources Research,
692 49(6), 3487–3503. https://doi.org/10.1002/wrcr.20299
693 Goldscheider, N., Chen, Z., Auler, A. S., Bakalowicz, M., Broda, S., Drew, D., et al.
694 (2020). Global distribution of carbonate rocks and karst water resources. *Hydrogeology Journal*,
695 *28*(5), 1661–1677. https://doi.org/10.1007/s10040-020-02139-5
696 Hartmann, A., Jasechko, S., Gleeson, T., Wada, Y., Andreo, B., Barberá, J. A., et al.
697 (2021). Risk of groundwater contamination widely underestimated because of fast flow into
698 aquifers. *Proceedings of the National Academy of Sciences*, *118*(20).
699 https://doi.org/10.1073/pnas.2024492118
700 Hauns, M., Jeannin, P.-Y., & Atteia, O. (2001). Dispersion, retardation and scale effect in
701 tracer breakthrough curves in karst conduits. Journal of Hydrology, 241(3–4), 177–193.
702 https://doi.org/10.1016/S0022-1694(00)00366-8
703 Heathwaite, A. L., & Bieroza, M. (2021). Fingerprinting hydrological and
704 biogeochemical drivers of freshwater quality. Hydrological Processes, 35(1), e13973.

Hess, J. W., & White, W. B. (1988). Storm response of the karstic carbonate aquifer of southcentral Kentucky. Journal of Hydrology, 99(3–4), 235–252. https://doi.org/10.1016/0022-1694(88)90051-0

House, W. A., & Warwick, M. S. (1998). Hysteresis of the solute concentration/discharge relationship in rivers during storms. Water Research, 32(8), 2279–2290. https://doi.org/10.1016/S0043-1354(97)00473-9

Huebsch, M., Fenton, O., Horan, B., Hennessy, D., Richards, K. G., Jordan, P., Goldscheider, N., Butscher, C., and Blum, P. (2014). Mobilisation or dilution? Nitrate response of karst springs to high rainfall events, Hydrol. Earth Syst. Sci., 18, 4423–4435, https://doi.org/10.5194/hess-18-4423-2014

Jerome Morrissey, P., McCormack, T., Naughton, O., Meredith Johnston, P., & William Gill, L. (2020). Modelling groundwater flooding in a lowland karst catchment. *Journal of Hydrology*, *580*, 124361. https://doi.org/10.1016/j.jhydrol.2019.124361

Knapp, J. L. A., von Freyberg, J., Studer, B., Kiewiet, L., & Kirchner, J. W. (2020). Concentration–discharge relationships vary among hydrological events, reflecting differences in event characteristics. Hydrology and Earth System Sciences, 24(5), 2561–2576. https://doi.org/10.5194/hess-24-2561-2020

Lambán, L. J., Jódar, J., Custodio, E., Soler, A., Sapriza, G., & Soto, R. (2015). Isotopic and hydrogeochemical characterization of high-altitude karst aquifers in complex geological settings. The Ordesa and Monte Perdido National Park (Northern Spain) case study. Science of The Total Environment, 506–507, 466–479. https://doi.org/10.1016/j.scitotenv.2014.11.030

Le Mesnil, M., Charlier, J.-B., Moussa, R., Caballero, Y., & Dörfliger, N. (2020). Interbasin groundwater flow: Characterization, role of karst areas, impact on annual water

728 balance and flood processes. Journal of Hydrology, 585, 124583.
729 https://doi.org/10.1016/j.jhydrol.2020.124583
730 Le Mesnil, M., Moussa, R., Charlier, J.-B., Caballero, Y. (2021). Impact of karst areas on
731 runoff generation, lateral flow and interbasin groundwater flow at the storm-event timescale.
732 Hydrol. Earth Syst. Sci. 25, 1259–1282. https://doi.org/10.5194/hess-25-1259-2021
733 Liu, Z., Li, Q., Sun, H., & Wang, J. (2007). Seasonal, diurnal and storm-scale
734 hydrochemical variations of typical epikarst springs in subtropical karst areas of SW China: Soil
735 CO2 and dilution effects. Journal of Hydrology, 337(1–2), 207–223.
736 https://doi.org/10.1016/j.jhydrol.2007.01.034
737 Lloyd, C. E. M., Freer, J. E., Johnes, P. J., & Collins, A. L. (2016). Technical Note:
738 Testing an improved index for analysing storm discharge–concentration hysteresis. Hydrology
739 and Earth System Sciences, 20(2), 625–632. https://doi.org/10.5194/hess-20-625-2016
740 Lloyd, J. W., & Heathcote, J. A. (1985). Natural inorganic hydrochemistry in relation to
741 ground water. Retrieved from https://www.osti.gov/biblio/6026514
742 López-Chicano, M., Calvache, M. L., Martín-Rosales, W., & Gisbert, J. (2002).
743 Conditioning factors in flooding of karstic poljes—the case of the Zafarraya polje (South Spain).
744 CATENA, 49(4), 331–352. https://doi.org/10.1016/S0341-8162(02)00053-X
745 Luhmann, A. J., Covington, M. D., Alexander, S. C., Chai, S. Y., Schwartz, B. F.,
746 Groten, J. T., & Alexander, E. C. (2012). Comparing conservative and nonconservative tracers in
747 karst and using them to estimate flow path geometry. Journal of Hydrology, 448–449, 201–211.
748 https://doi.org/10.1016/j.jhydrol.2012.04.044

Mallard, J., McGlynn, B., & Covino, T. (2014). Lateral inflows, stream-groundwater exchange, and network geometry influence stream water composition. Water Resources Research, 50(6), 4603–4623. https://doi.org/10.1002/2013WR014944

Maréchal, J. C., Ladouche, B., & Dörfliger, N. (2008). Karst flash flooding in a Mediterranean karst, the example of Fontaine de Nîmes. Engineering Geology, 99(3–4), 138–146. https://doi.org/10.1016/j.enggeo.2007.11.013

Massei, N., Mahler, B. J., Bakalowicz, M., Fournier, M., & Dupont, J. P. (2007). Quantitative Interpretation of Specific Conductance Frequency Distributions in Karst. Ground Water, 45(3), 288–293. https://doi.org/10.1111/j.1745-6584.2006.00291.x

Mayaud, C., Gabrovšek, F., Blatnik, M., Kogovšek, B., Petrič, M., & Ravbar, N. (2019). Understanding flooding in poljes: A modelling perspective. *Journal of Hydrology*, *575*, 874–889. https://doi.org/10.1016/j.jhydrol.2019.04.092

Moussa, R. (1996). Analytical Hayami solution for the diffusive wave flood routing problem with lateral inflow. Hydrological Processes, 10(9), 1209–1227. https://doi.org/10.1002/(SICI)1099-1085(199609)10:9<1209::AID-HYP380>3.0.CO;2-2

Moussa, R., & Bocquillon, C. (1996). Criteria for the choice of flood-routing methods in natural channels. Journal of Hydrology, 186(1–4), 1–30. https://doi.org/10.1016/S0022-1694(96)03045-4

Moussa, R., & Bocquillon, C. (2009). On the use of the diffusive wave for modelling extreme flood events with overbank flow in the floodplain. Journal of Hydrology, 374(1–2), 116–135. https://doi.org/10.1016/j.jhydrol.2009.06.006

Moussa, R., & Majdalani, S. (2019). Evaluating lateral flow in an experimental channel using the diffusive wave inverse problem. Advances in Water Resources, 127, 120–133. https://doi.org/10.1016/j.advwatres.2019.03.009

Neira, J. M. T., Tallec, G., Andreassian, V., & Mouchel, J. M. (2020). A combined mixing model for high-frequency concentration–discharge relationships. Journal of Hydrology, 591, 125559.

Peyraube, N., Lastennet, R., Denis, A., Minvielle, S., Houillon, N., Lorette, G., et al. (2019). SIc–Abacus: An in–situ tool for estimating SIc and Pco2 in the context of carbonate karst. Journal of Hydrology, 568, 891–903. https://doi.org/10.1016/j.jhydrol.2018.11.042

Pinault, J.-L., Amraoui, N., & Golaz, C. (2005). Groundwater-induced flooding in macropore-dominated hydrological system in the context of climate changes. Water Resources Research, 41(5). https://doi.org/10.1029/2004WR003169

Pronk, M., Goldscheider, N., Zopfi, J., & Zwahlen, F. (2009). Percolation and Particle Transport in the Unsaturated Zone of a Karst Aquifer. Ground Water, 47(3), 361–369. https://doi.org/10.1111/j.1745-6584.2008.00509.x

Ravbar, N., Engelhardt, I., & Goldscheider, N. (2011). Anomalous behaviour of specific electrical conductivity at a karst spring induced by variable catchment boundaries: the case of the Podstenjšek spring, Slovenia. Hydrological Processes, 25(13), 2130-2140.

Ribolzi, O., Andrieux, P., Valles, V., Bouzigues, R., Bariac, T., & Voltz, M. (2000). Contribution of groundwater and overland ¯ows to storm ¯ow generation in a cultivated Mediterranean catchment. Quanti®cation by natural chemical tracing. Journal of Hydrology, 17.

Rose, L. A., Karwan, D. L., & Godsey, S. E. (2018). Concentration-discharge relationships describe solute and sediment mobilization, reaction, and transport at event and

longer timescales. Hydrological Processes, 32(18), 2829–2844. https://doi.org/10.1002/hyp.13235

Rose, S. (2003). Comparative solute–discharge hysteresis analysis for an urbanized and a 'control basin' in the Georgia (USA) Piedmont. Journal of Hydrology, 284(1–4), 45–56. https://doi.org/10.1016/j.jhydrol.2003.07.001

Runkel, R. L. (1996). Solution of the Advection-Dispersion Equation: Continuous Load of Finite Duration. Journal of Environmental Engineering, 122(9), 830–832. https://doi.org/10.1061/(ASCE)0733-9372(1996)122:9(830)

Singh, V. P. (2002). Is hydrology kinematic? Hydrological Processes, 16(3), 667–716. https://doi.org/10.1002/hyp.306

Todini, E. (1996). The ARNO rainfall—runoff model. Journal of Hydrology, 175(1–4), 339–382. https://doi.org/10.1016/S0022-1694(96)80016-3

Toran, L., & Reisch, C. E. (2012). Using Stormwater Hysteresis to Characterize Karst Spring Discharge. Ground Water, no-no. https://doi.org/10.1111/j.1745-6584.2012.00984.x

Tritz, S., Guinot, V., & Jourde, H. (2011). Modelling the behaviour of a karst system catchment using non-linear hysteretic conceptual model. Journal of Hydrology, 397(3–4), 250–262. https://doi.org/10.1016/j.jhydrol.2010.12.001

Vaughan, M. C. H., Bowden, W. B., Shanley, J. B., Vermilyea, A., Sleeper, R., Gold, A. J., et al. (2017). High-frequency dissolved organic carbon and nitrate measurements reveal differences in storm hysteresis and loading in relation to land cover and seasonality. Water Resources Research, 53(7), 5345–5363. https://doi.org/10.1002/2017WR020491

814 Vidal, J.-P., Martin, E., Franchistéguy, L., Baillon, M., & Soubeyroux, J.-M. (2010). A
815 50-year high-resolution atmospheric reanalysis over France with the Safran system. International
816 Journal of Climatology, 30(11), 1627–1644. https://doi.org/10.1002/joc.2003
817 Zhang, R., Chen, X., Zhang, Z., & Soulsby, C. (2020). Using hysteretic behaviour and
818 hydrograph classification to identify hydrological function across the "hillslope–depression–
819 stream" continuum in a karst catchment. Hydrological Processes, 34(16), 3464–3480.
820 https://doi.org/10.1002/hyp.13793
821

822 Appendix: Hayami analytical resolution of DWE and ADE

823 **Diffusive wave equation**

824 An inverse modelling approach is adopted for simulating lateral flow between two
825 gauging stations. This approach simulates the lateral flow Q_L, based on measurements from two
826 gauging stations Q_I and Q_O.

827 The diffusive wave equation (DWE), accounting for lateral flow, is an approximation of
828 the St-Venant equation that can be written as:

829 $$\frac{\partial Q}{\partial t} + c(Q)\left[\frac{\partial Q}{\partial x} - q\right] - D(Q)\left[\frac{\partial^2 Q}{\partial x^2} - \frac{\partial q}{\partial x}\right] = 0 \quad \text{(A1)}$$

830 where x [L] is the length along the channel, t [T] is the time, and celerity c(Q) [LT^{-1}] and
831 diffusivity D(Q)[L^2T^{-1}] are functions of the discharge Q [L^3T^{-1}]. The term q(x,t) [L^2T^{-1}]
832 represents the lateral flow distribution. The lateral hydrograph $Q_L(t)$ is given by:

833 $$Q_L(t) = \int_0^l q(x,t)dx \quad \text{(A2)}$$

834 with l [L] the channel length.

Moussa (1996) extended the solution of the DWE under Hayami's hypotheses (semi-infinite channel, c(Q) and D(Q) constant) to the case where lateral flow is uniformly distributed along the channel. Let I(t) and O(t) be the inlet flow minus baseflow and the outlet flow minus baseflow, respectively:

$$O(t) = \varphi(t) + [I(t) - \varphi(t)] * K(t) \quad \text{(A3)}$$

with K(t) the Hayami Kernel function defined as:

$$K(t) = \frac{l}{2(\pi D)^{1/2}} \frac{e^{\left[\frac{Cl}{4D}\left(2-\frac{l}{Ct}-\frac{Ct}{l}\right)\right]}}{t^{3/2}} \quad \text{(A4)}$$

and

$$\varphi(t) = \frac{c}{l}\int_0^t [Q_L(\theta) - Q_L(0)]d\theta \quad \text{(A5)}$$

The inverse problem

Under Hayami's conditions and assuming that lateral flow is uniformly distributed along the channel, Moussa (1996) proposed a solution of the inverse problem; this enables evaluation of the temporal distribution of lateral flow $Q_L(t)$ over the channel reach by knowing I(t) and O(t). Knowing c, D and l, the lateral flow can be calculated using the following procedure:

$$L(t) = O(t) - I(t) * K(t) \quad \text{(A6)}$$

$$K^i(t) = K * K *. \; . \; .* K \quad (i \; times) \quad \text{(A7)}$$

$$\varphi(t) = L(t) + L(t)\sum_{i=1}^{\infty} K^i(t) \quad \text{(A8)}$$

and finally the lateral flow $Q_{L,c}(t)$

$$Q_{L,c}(t) = Q_L(0) + \frac{l}{c}\frac{d\varphi}{dt} \quad \text{(A9)}$$

The DWE equation has two free parameters, namely celerity c ($m.s^{-1}$) and diffusivity D ($m^2.s^{-1}$) of the flood wave. Sensitivity analysis of the DWE to the two parameters is largely

856 available in the literature, showing that it is more sensitive to parameter c than D (Moussa and
857 Bocquillon, 1996; Cholet al., 2017; Charlier et al., 2019). Therefore, c is assumed equal to time
858 delay between peak discharges of Q_I and $Q_{O,}$ and D is fixed in accordance with stream
859 characterization proposed by Todini (1996). The DWE solution was validated experimentally
860 under controlled conditions (Moussa and Majdalani, 2019), and has been implemented on natural
861 karst catchments (Charlier et al., 2015, 2019; Cholet et al., 2017).
862 The lateral mass fluxes M_L simulation by the ADE is done using the same analytical
863 solution than DWE, as under some hypotheses, the physical equations of both the DWE and the
864 ADE can lead to similar mathematical expressions. M_L is simulated using M_I and M_O.

Figure 1: Framework of the general methodology at the scales of nested catchments and river reaches. Spatial scales: topographic catchment vs. river reach. Monitored data: discharge (Q: Q_I at Inlet in light blue and Q_O at Outlet in dark blue) and electrical conductivity (EC: EC_I at I in light orange and EC_O at O in dark orange) during a storm event. Data processing: EC-Q hysteresis loop at the outlet O characterized by its slope (s) and hysteresis index (HI) versus inverse modelling of lateral Q_L and EC_L using the diffusive wave equation with Q_I, Q_O, EC_I and EC_O. PEW: Pre-Event Water; EW: Event Water.

Figure 2: Calculation of local HI_i indexes on an illustrative storm event (Chenecey, Jura, France, 18 September 2016).

Figure 3: EC-Q loop classification, adapted from Evans and Davies (1998), and corresponding streamflow contributions (PEW: pre-event water, EW: event water) in the case of catchments where EC is positively corelated to water residence time (e.g. karst areas), and initial EC is superior to EC value of EW end-member.

Figure 4: Location of gauging stations and river network in the studied catchments. Background: geological map. Karst outcrops are located on limestone areas .

Figure 5: Boxplots of mean EC values during storm events and corresponding annual values (circles) for Loue catchment (a) and Cèze catchment (b).

Figure 6: Examples of EC and Q variations recorded during storm events, with associated EC-Q loops and classifications. Slopes are expressed in $\mu S.cm^{-1}.m^{-3}.s$. HI is dimensionless. a: Nans (Loue), 14 March 2017; b: Ouhans (Loue), 3 June 2017; c: Montclus (Cèze), 20 October 2019; d: Laroque (Cèze), 22 November 2019.

Figure 7: Distribution of slope (a, b) and HI (c, d) values for the Loue (a, c) and Cèze (b, d) catchments, grouped by season. Black crosses indicate no available data.

Figure 8: Variations of input, output and lateral simulated discharge (a, c) and electrical conductivity (c, d). Example on the Loue catchment Ouhans-Vuillafans reach, March 2017 (left) and on the Cèze catchment Tharaux-Montclus reach, October 2019 (right).

Figure 9: Distribution of simulated lateral flow EC on Loue (a) and Cèze (b) reaches, mean values calculated around the peak of lateral inflow, with pre-event water (PEW) and event-water (EW) EC end-member values in dashed lines. From left to right, plotted reaches are from upstream to downstream.

Figure 10: Conceptual model of main flood processes and water origin seasonality in the Loue catchment (a and b) and the Cèze catchment (c and d), with hysteresis loop types, associated schematic hydrographs and main patterns of spatial variability (e and f). Dark blue: event water, green: pre-event water, light blue: total streamflow. Bottom triangles describe dominant water origin spatial variability from headwaters to outlet.

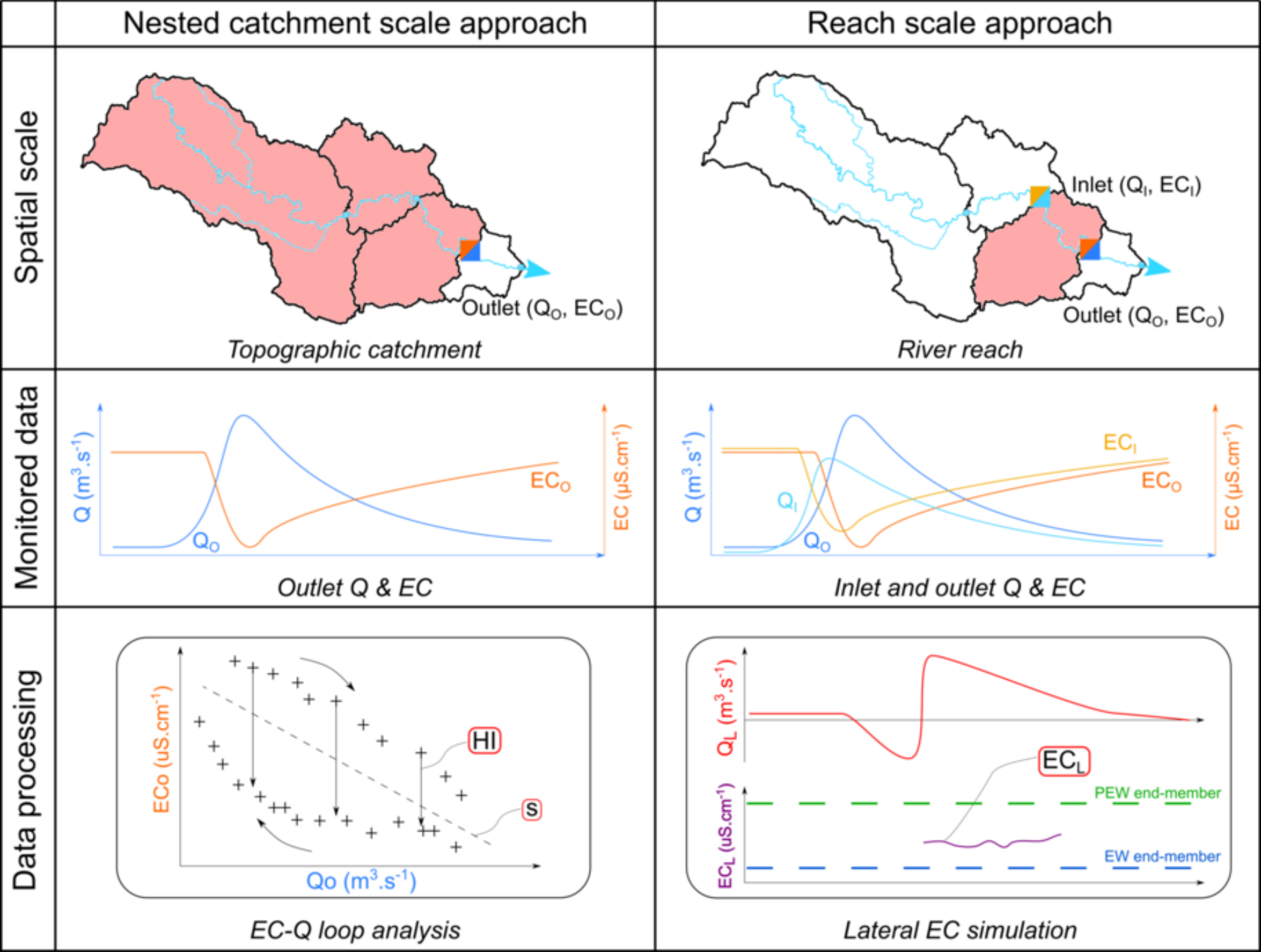
Nested catchment scale approach
Reach scale approach
Spatial scale
Outlet (Q_O, EC_O)
Topographic catchment
Inlet (Q_I, EC_I)
Outlet (Q_O, EC_O)
River reach
Monitored data
Q ($m^3.s^{-1}$)
Q_O
EC_O
EC ($\mu S.cm^{-1}$)
Outlet Q & EC
EC_I
Q_I
Inlet and outlet Q & EC
Data processing
ECo (uS.cm^{-1})
Qo ($m^3.s^{-1}$)
HI
S
EC-Q loop analysis
Q_L ($m^3.s^{-1}$)
EC_L
EC_L (uS.cm^{-1})
PEW end-member
EW end-member
Lateral EC simulation

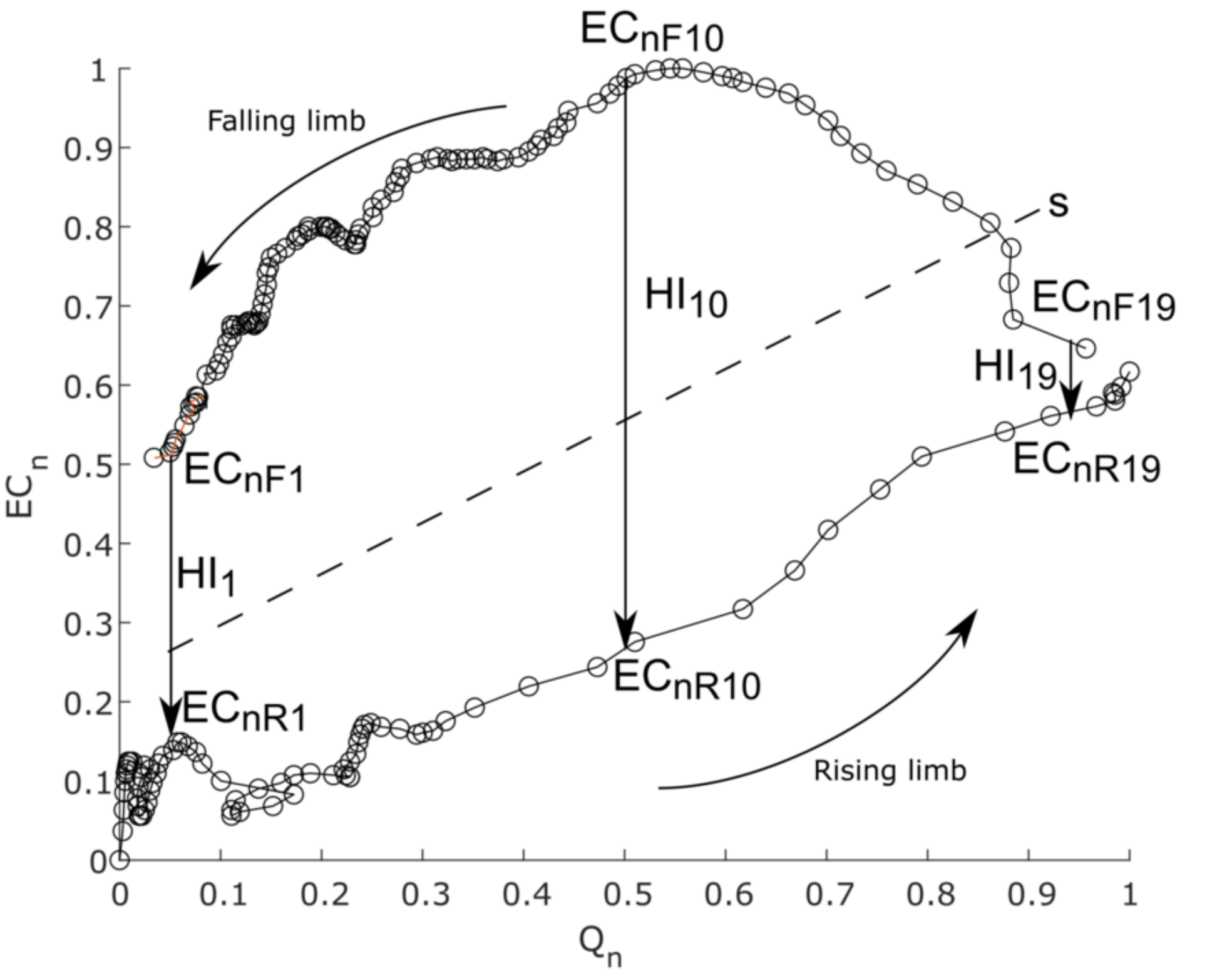
ECnF10
Falling limb
s
HI10
ECnF19
HI19
ECnR19
ECnF1
HI1
ECnR1
ECnR10
Rising limb
ECn
Qn
0
0.1
0.2
0.3
0.4
0.5
0.6
0.7
0.8
0.9
1

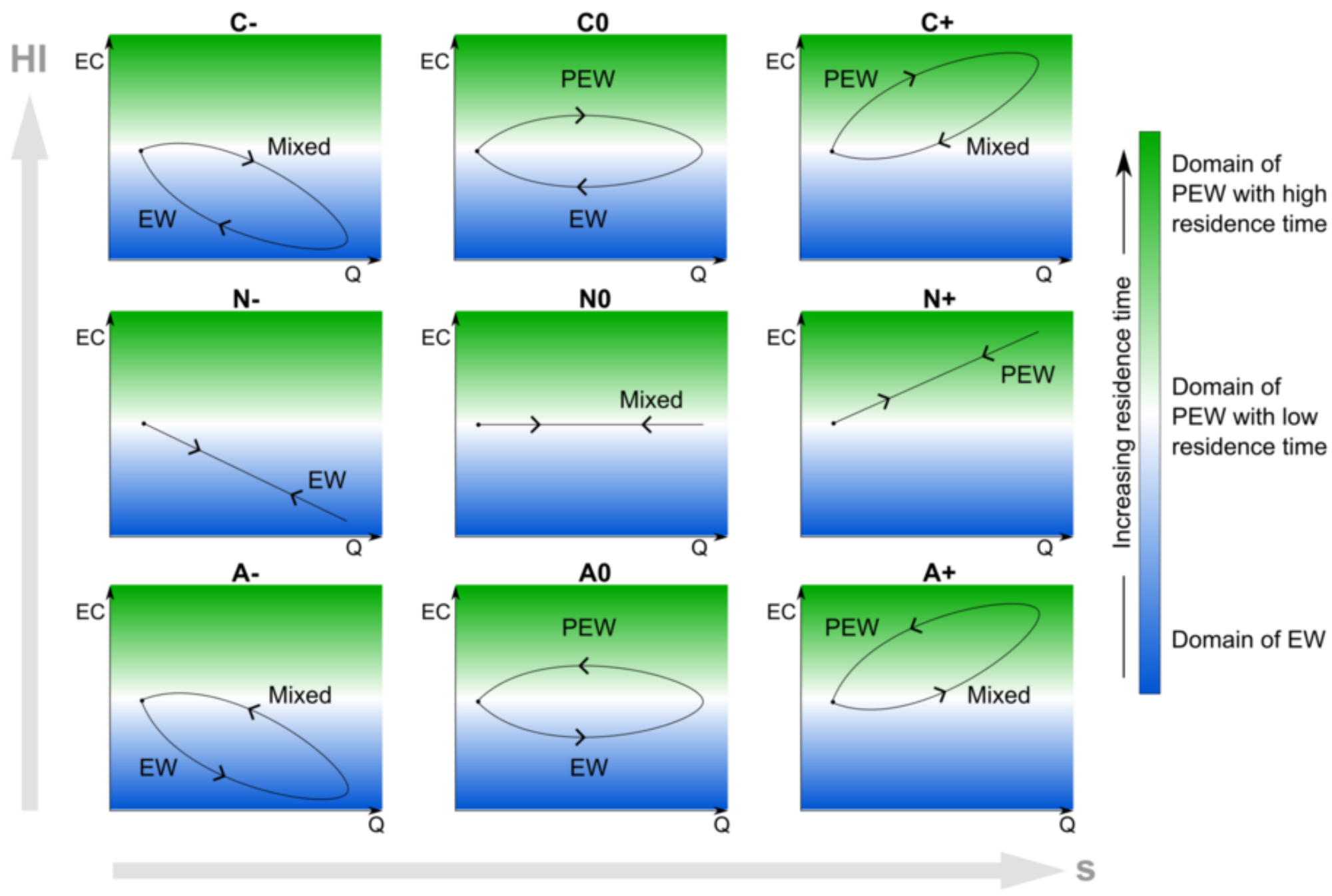
HI
C-
EC
Mixed
EW
Q
C0
EC
PEW
EW
Q
C+
EC
PEW
Mixed
Q
N-
EC
EW
Q
N0
EC
Mixed
Q
N+
EC
PEW
Q
A-
EC
Mixed
EW
Q
A0
EC
PEW
EW
Q
A+
EC
PEW
Mixed
Q
S
Increasing residence time
Domain of PEW with high residence time
Domain of PEW with low residence time
Domain of EW

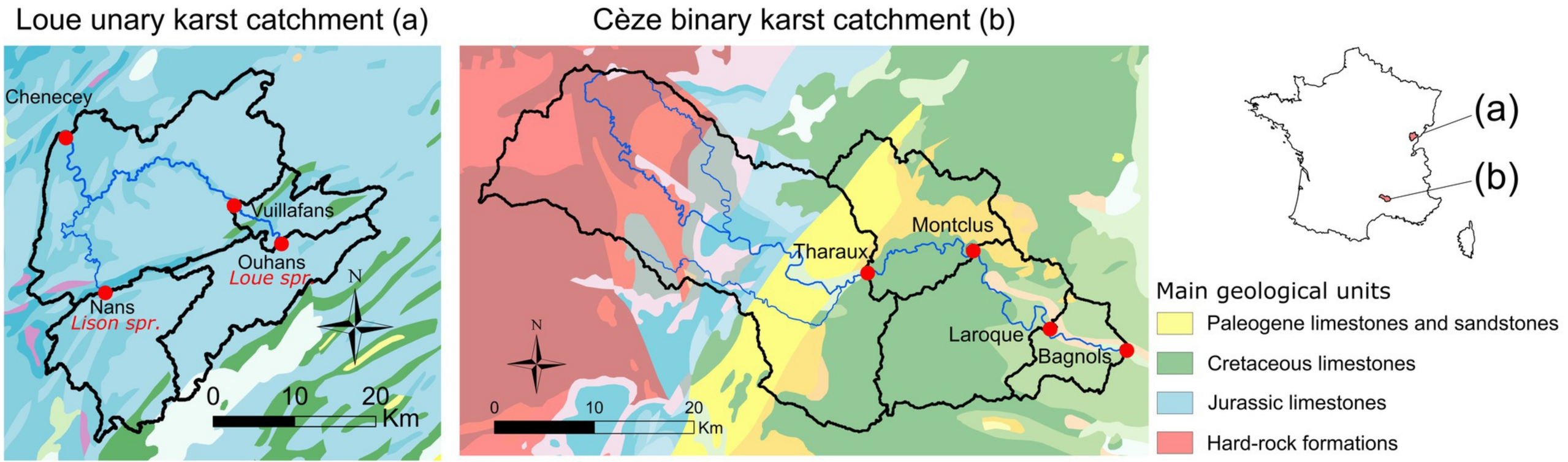
Loue unary karst catchment (a)
Chenecey
Vuillafans
Ouhans
Loue spr.
Nans
Lison spr.
N
0
10
20
Km
Cèze binary karst catchment (b)
Montclus
Tharaux
Laroque
Bagnols
N
0
10
20
Km
(a)
(b)
Main geological units
Paleogene limestones and sandstones
Cretaceous limestones
Jurassic limestones
Hard-rock formations

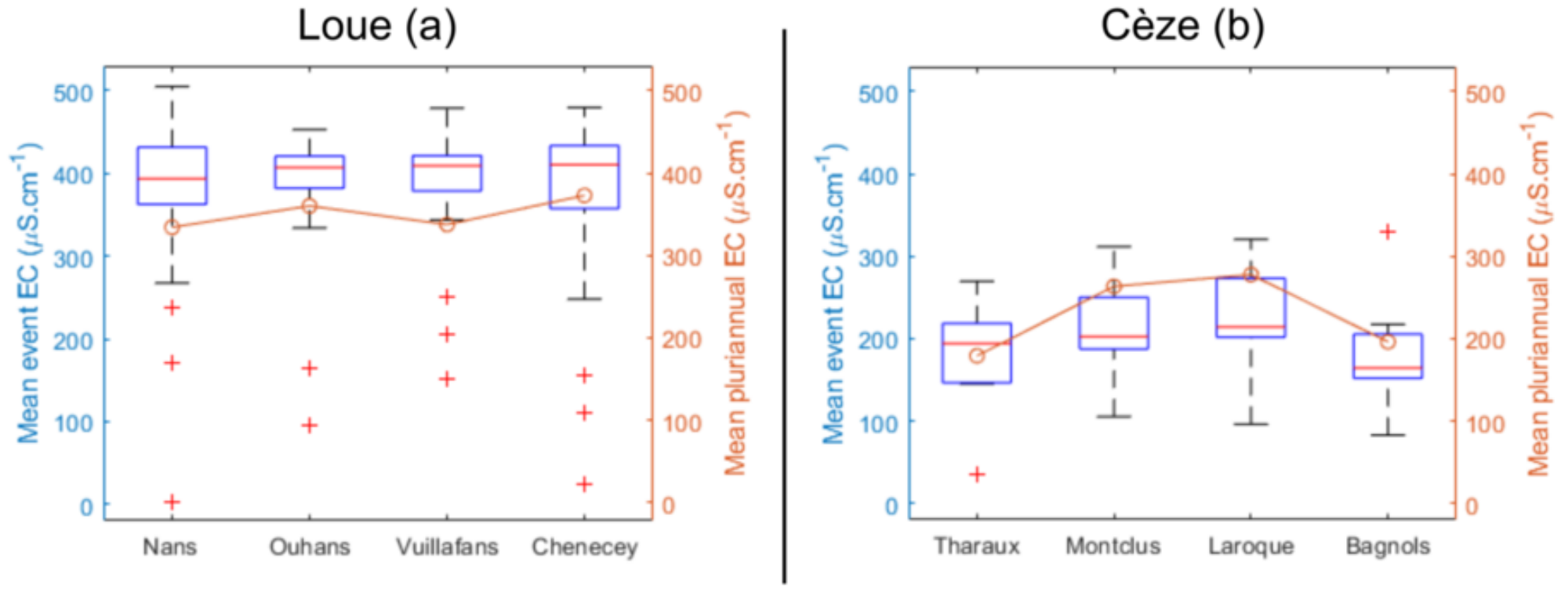
Loue (a)
Cèze (b)
Mean event EC (µS.cm-1)
Mean pluriannual EC (µS.cm-1)
0
100
200
300
400
500
Nans
Ouhans
Vuillafans
Chenecey
Tharaux
Montclus
Laroque
Bagnols

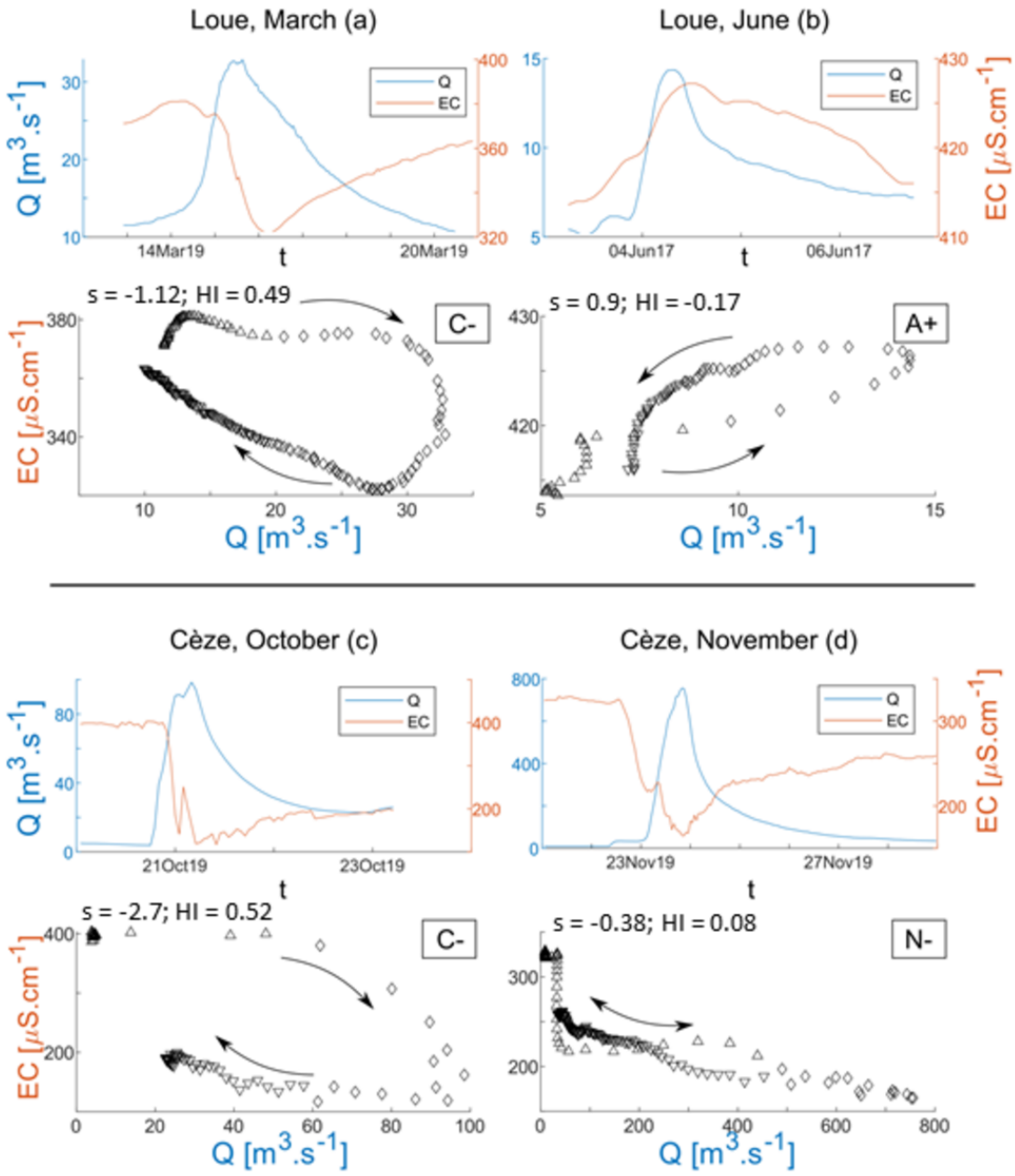
Loue, March (a)
Loue, June (b)
Q [m3.s-1]
EC [µS.cm-1]
Q
EC
14Mar19
20Mar19
04Jun17
06Jun17
t
s = -1.12; HI = 0.49
C-
s = 0.9; HI = -0.17
A+
Cèze, October (c)
Cèze, November (d)
21Oct19
23Oct19
23Nov19
27Nov19
s = -2.7; HI = 0.52
C-
s = -0.38; HI = 0.08
N-

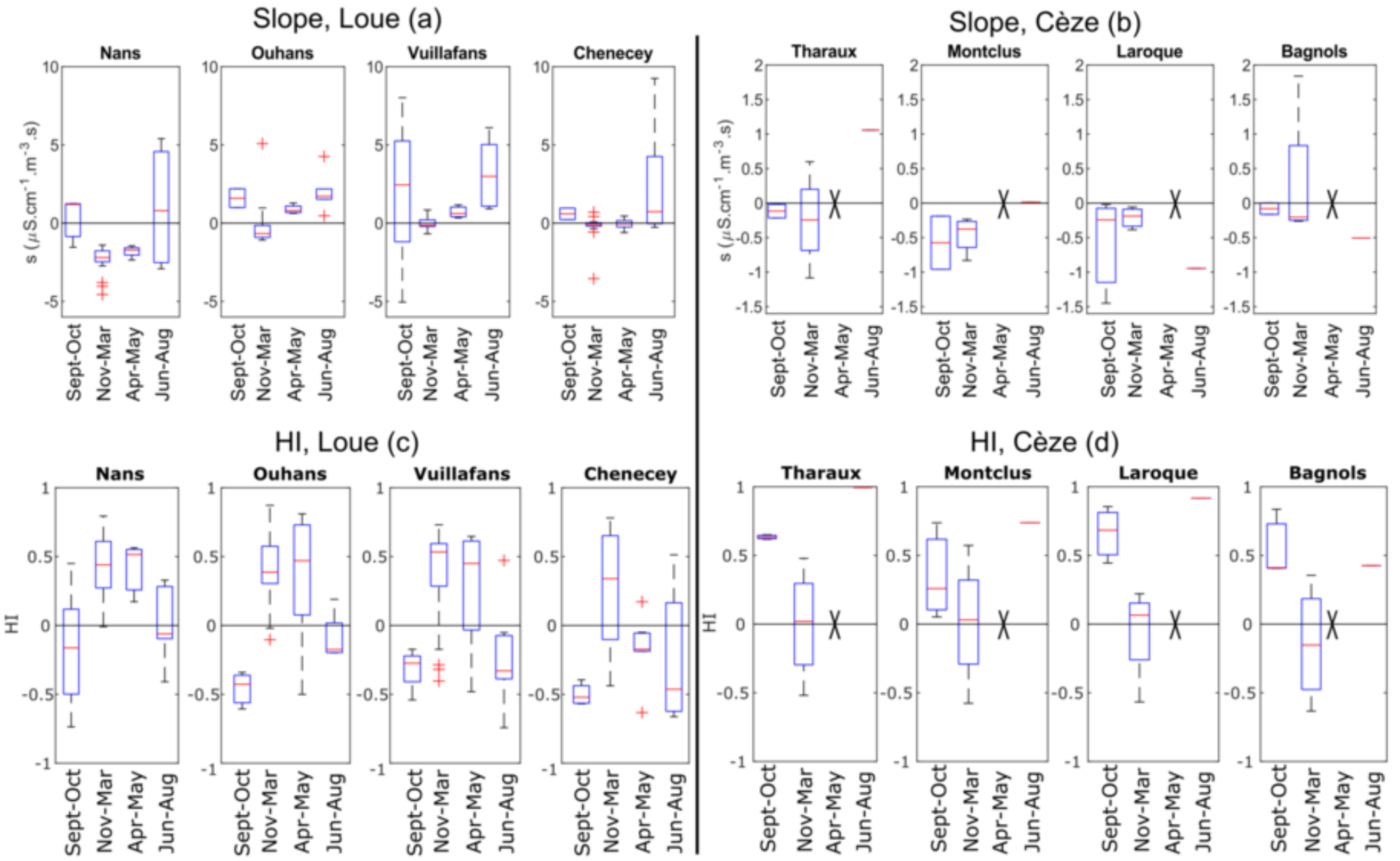
Slope, Loue (a)
Slope, Cèze (b)
HI, Loue (c)
HI, Cèze (d)
Nans
Ouhans
Vuillafans
Chenecey
Tharaux
Montclus
Laroque
Bagnols
s (µS.cm-1.m-3.s)
HI
Sept-Oct
Nov-Mar
Apr-May
Jun-Aug

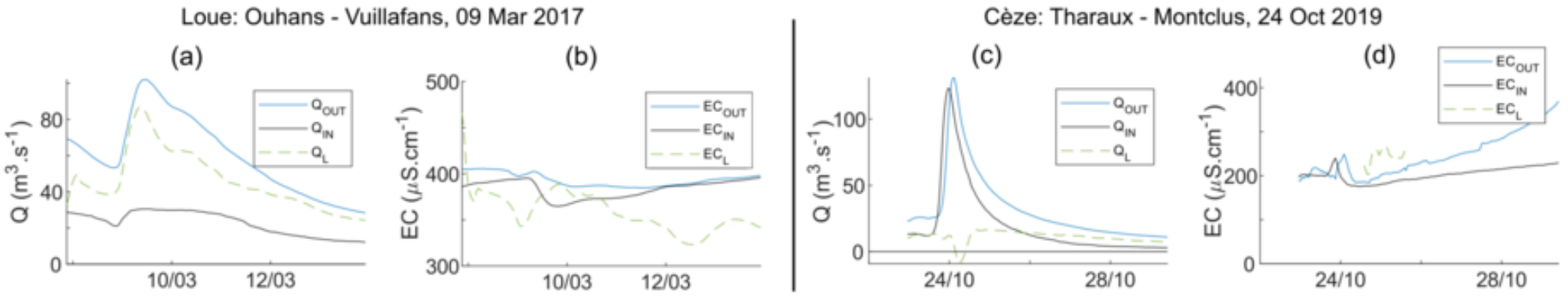
Loue: Ouhans - Vuillafans, 09 Mar 2017
Cèze: Tharaux - Montclus, 24 Oct 2019
(a)
(b)
(c)
(d)
Q (m3.s-1)
EC (µS.cm-1)
QOUT
QIN
QL
ECOUT
ECIN
ECL
10/03
12/03
24/10
28/10

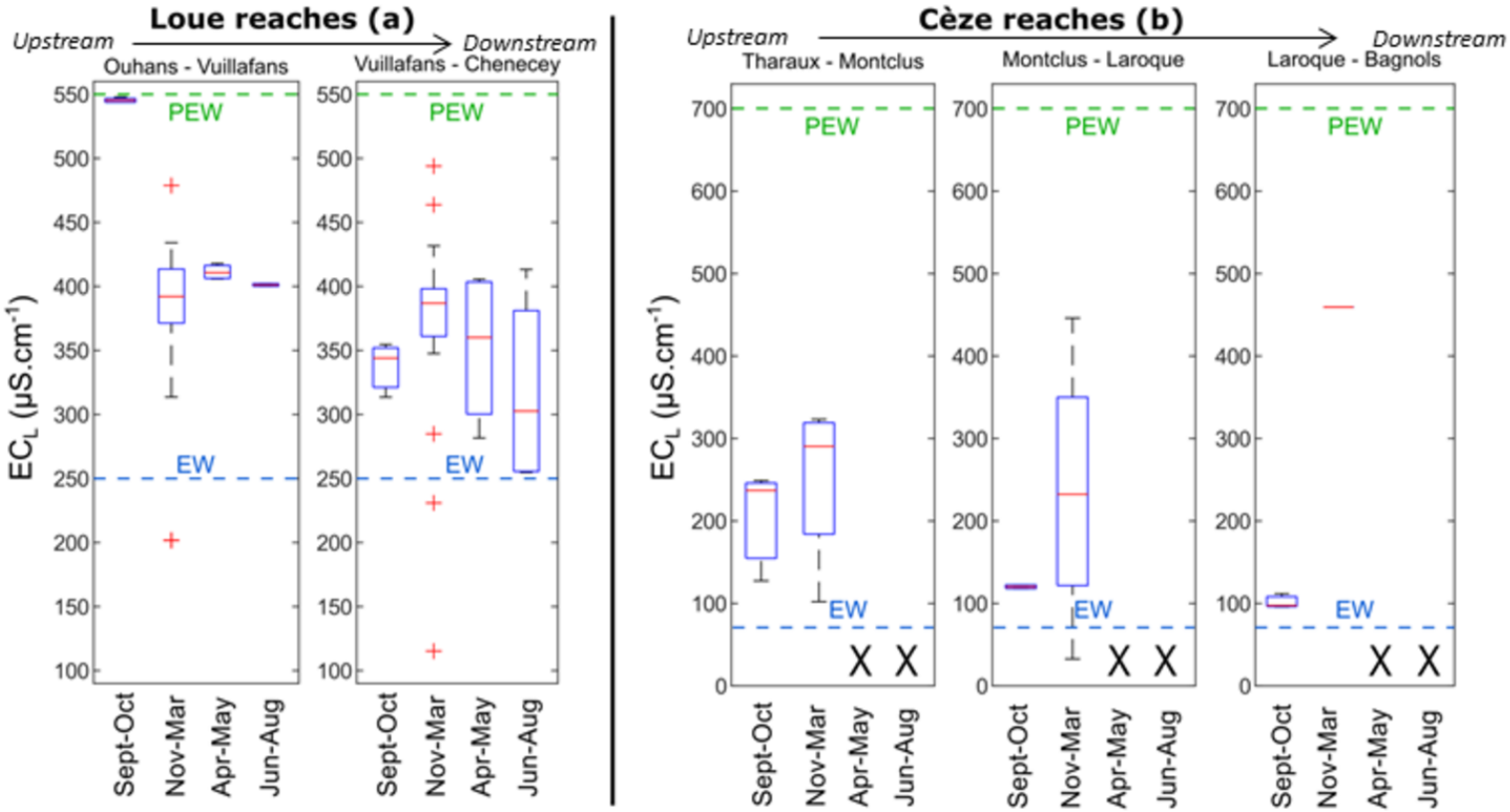
Loue reaches (a)
Upstream
Downstream
Ouhans - Vuillafans
Vuillafans - Chenecey
PEW
EW
EC_L (µS.cm^{-1})
Sept-Oct
Nov-Mar
Apr-May
Jun-Aug
Cèze reaches (b)
Upstream
Downstream
Tharaux - Montclus
Montclus - Laroque
Laroque - Bagnols
PEW
EW
EC_L (µS.cm^{-1})
Sept-Oct
Nov-Mar
Apr-May
Jun-Aug

Main storm hydrological processes

	Unary karst catchment, canyons and plateaus low surface runoff	Binary karst catchment, hard-rock and marly areas high surface runoff
November to May: high karst saturation rate	*Loue - Nov. to May (a)* 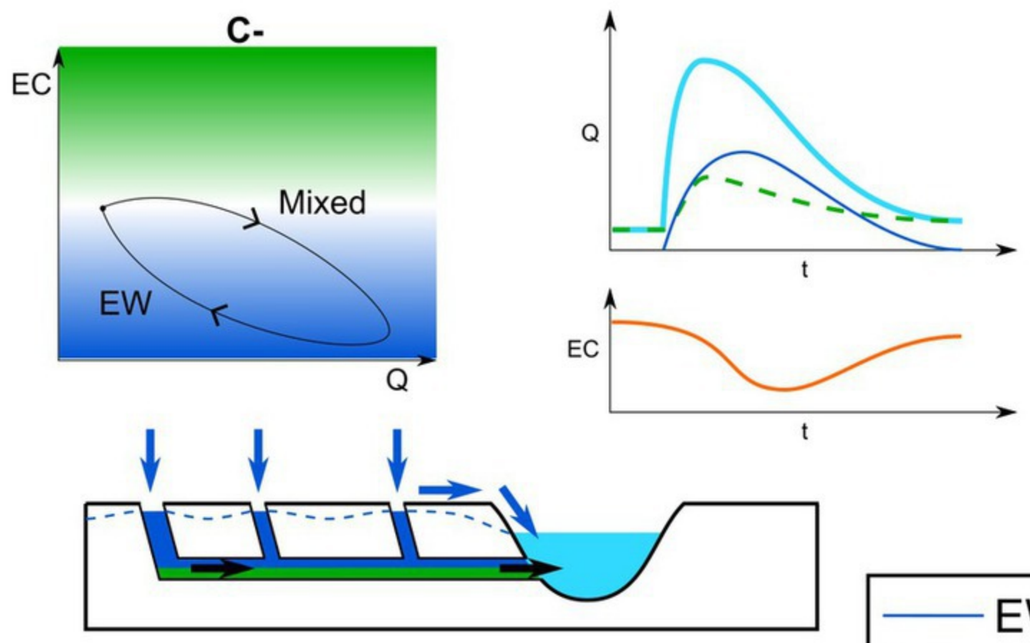	*Cèze - Nov. to May (c)* 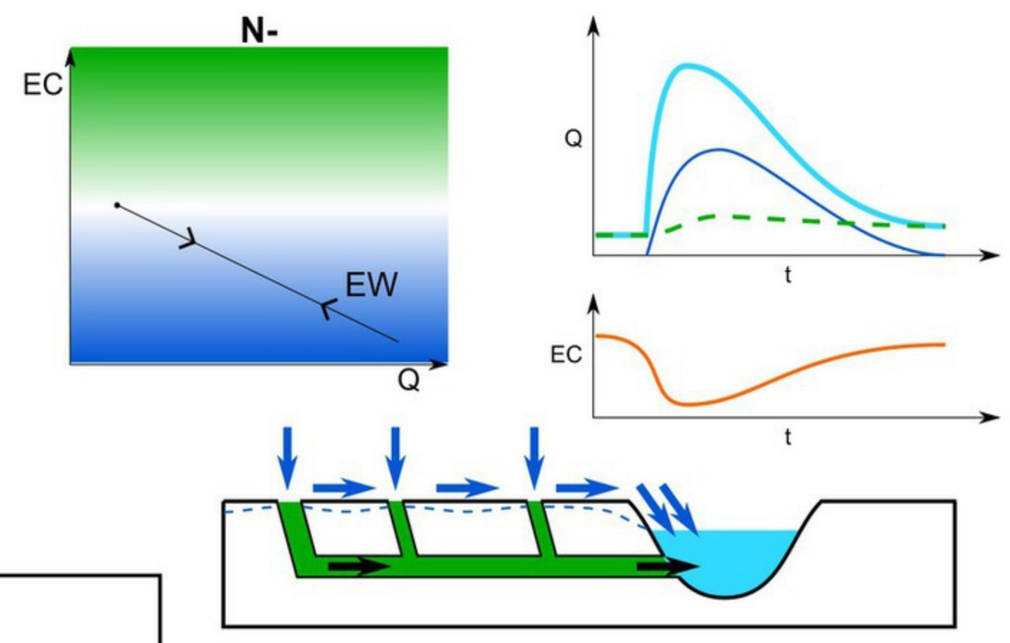
June to October: low karst saturation rate	*Loue - Jun. to Oct. (b)* 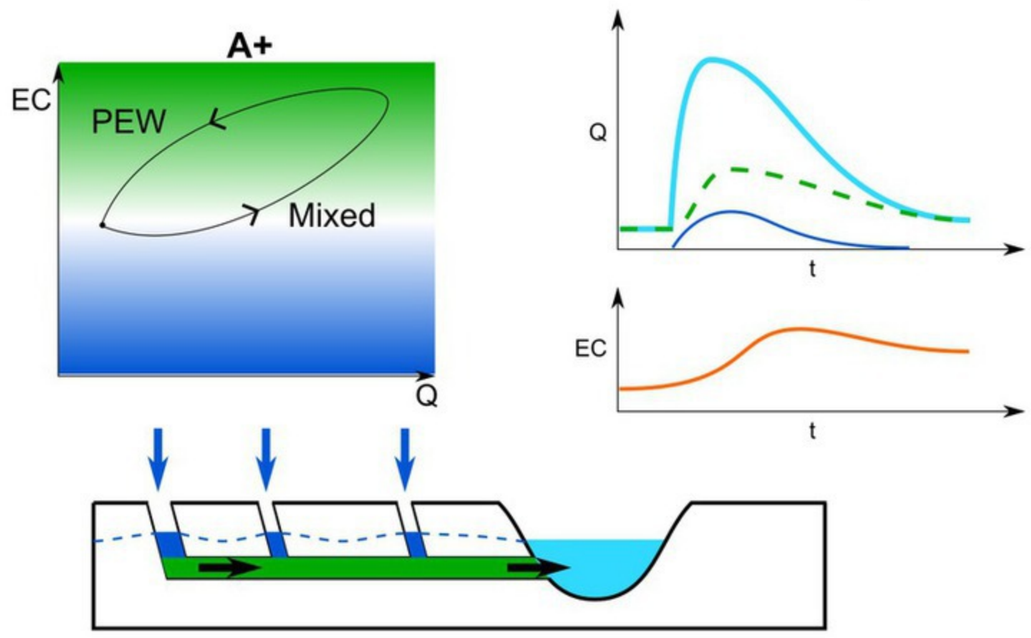	*Cèze - Jun. to Oct. (d)* 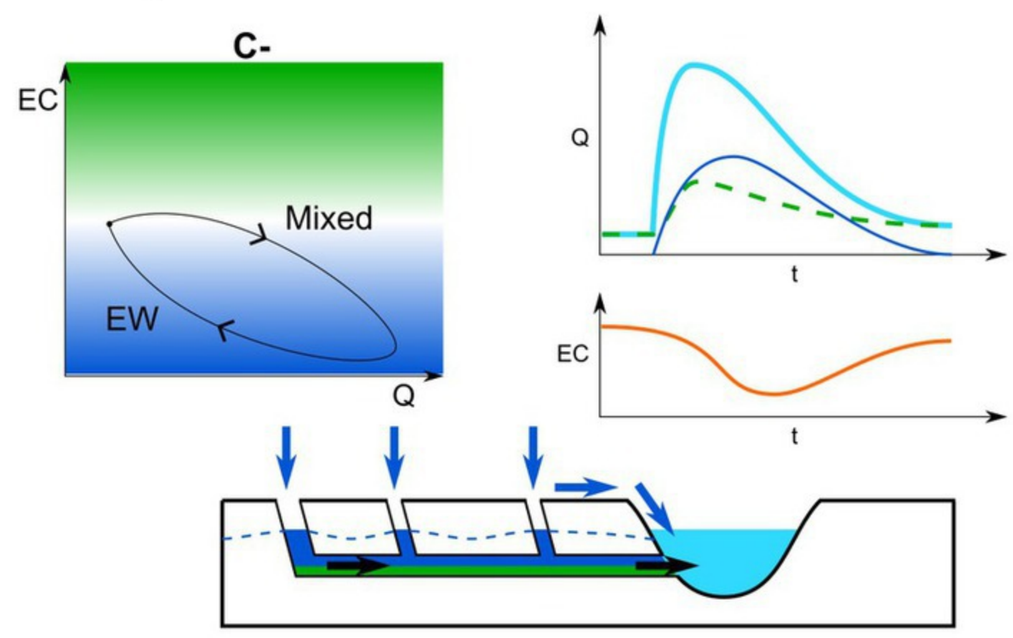

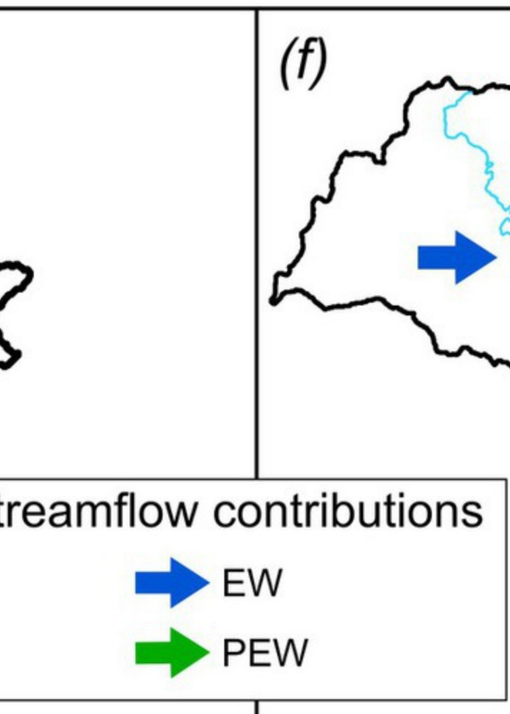

Intra-catchment water origin spatial variability

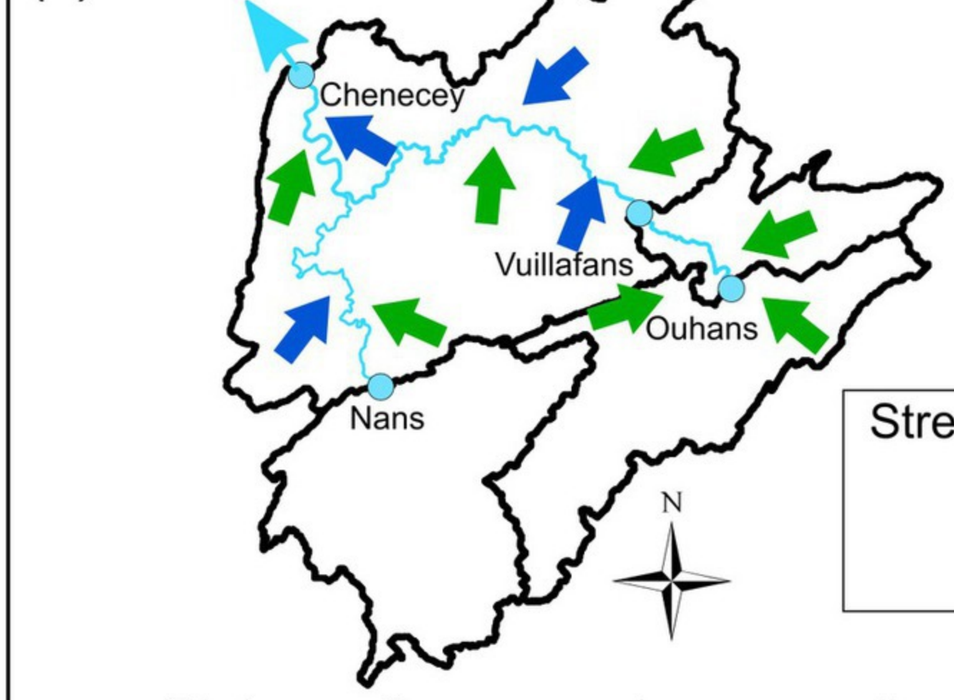

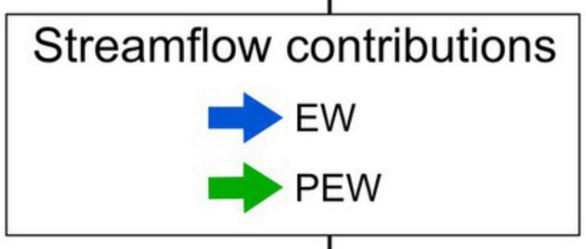

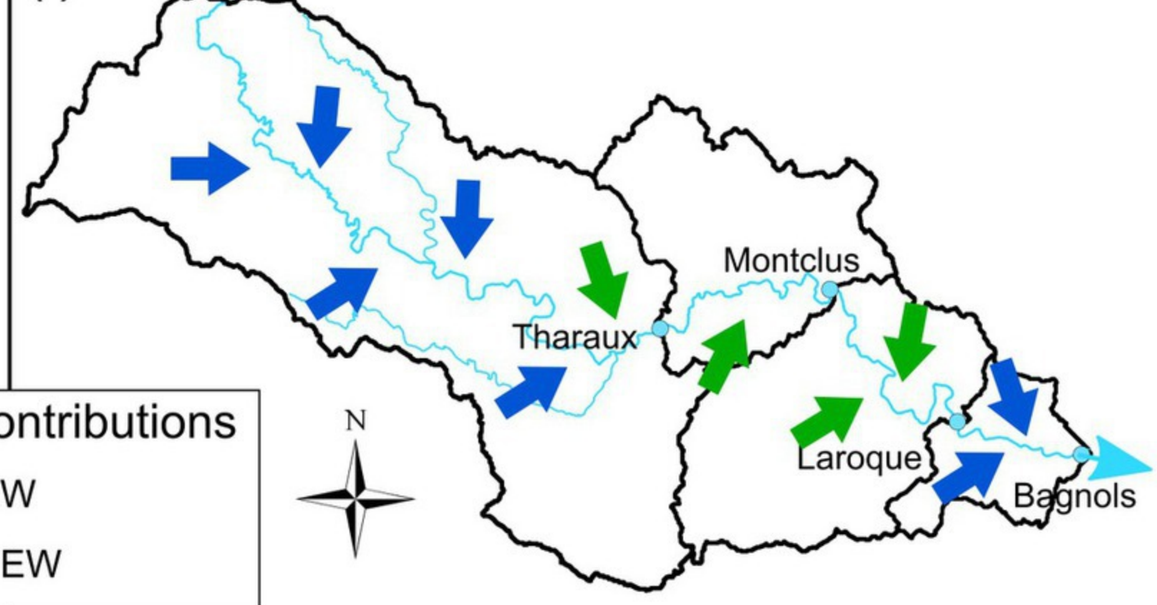

Plateaus & canyons to open valleys

Headwaters — *Outlet*

Increasing EW contribution

Hard rock to karst areas

Headwaters — *Outlet*

Increasing PEW contribution

	Nested catchment scale approach	Reach scale approach
Spatial scale	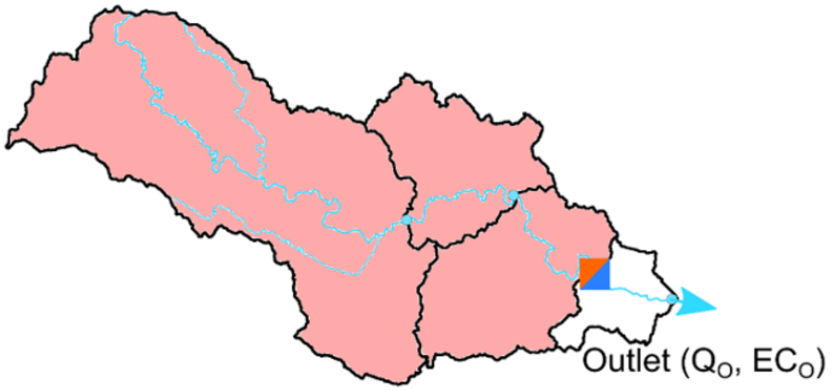 *Topographic catchment*	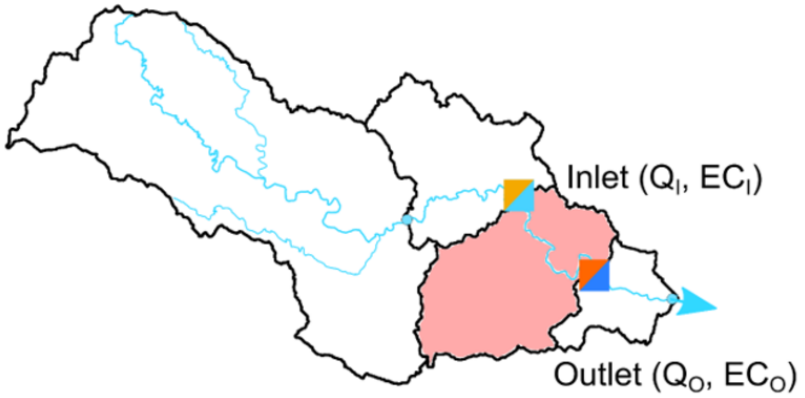 *River reach*
Methodology	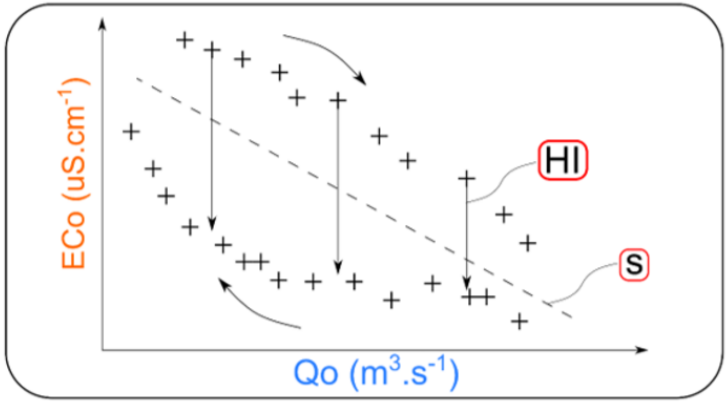 *EC-Q loop analysis*	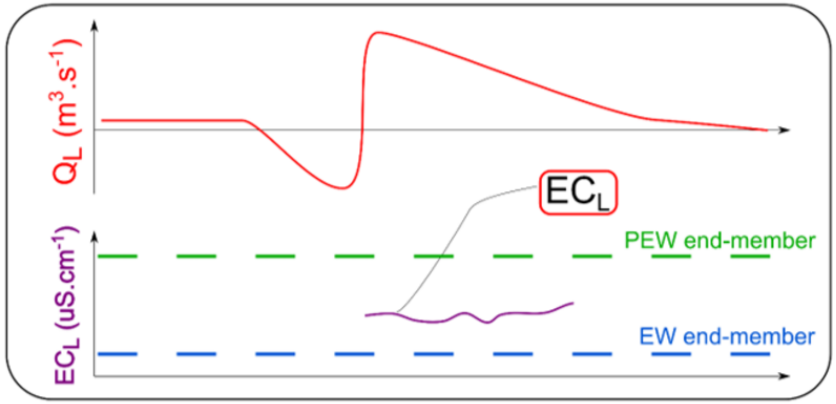 *Lateral EC simulation*
Results	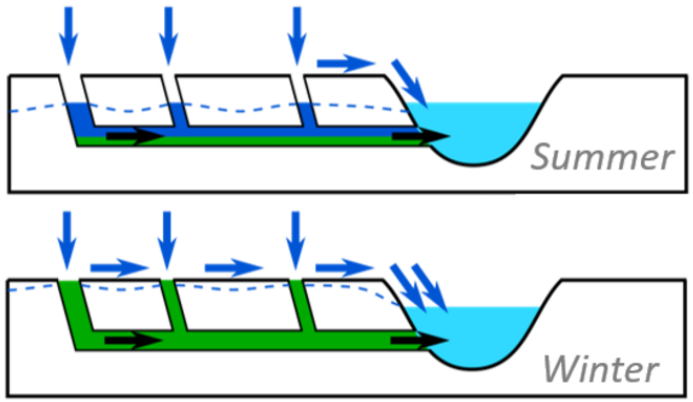 *Flood process seasonality*	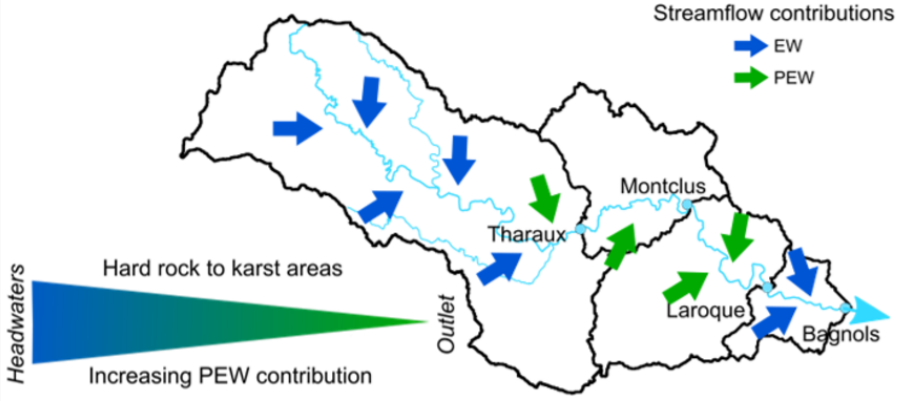 *Intra-catchment water origin variability*